Stony Brook University

The official electronic file of this thesis or dissertation is maintained by the University Libraries on behalf of The Graduate School at Stony Brook University.

Subgap Quasiparticle Transport and Low Frequency Critical Current Fluctuations in Nb/AlO$_\text{x}$/Nb Josephson Junctions

A Dissertation Presented

by

Shawn Paul Swan Pottorf

to

The Graduate School

in Partial Fulfillment of the Requirements

for the Degree of

Doctor of Philosophy

in

Physics

Stony Brook University

December 2007

Stony Brook University

The Graduate School

Shawn Paul Swan Pottorf

We, the dissertation committee for the above candidate for the Doctor of Philosophy degree, hereby recommend acceptance of this dissertation.

James E. Lukens – Dissertation Advisor
Professor, Department of Physics and Astronomy

Konstantin K. Likharev – Chairperson of Defense
Distinguished Professor, Department of Physics and Astronomy

Harold Metcalf
Distinguished Teaching Professor, Department of Physics and Astronomy

Serge Luryi
Distinguished Professor and Chair, Department of Electrical and Computer Engineering
Stony Brook University

This dissertation is accepted by the Graduate School.

Lawrence Martin
Dean of the Graduate School

Abstract of the Dissertation

Subgap Quasiparticle Transport and Low Frequency Critical Current Fluctuations in Nb/AlO$_\text{x}$/Nb Josephson Junctions

by

Shawn Paul Swan Pottorf

Doctor of Philosophy

in

Physics

Stony Brook University

2007

An ideal qubit for quantum computation is one that follows the DiVincenzo criteria[1]. Superconducting rf-SQUIDs meet part of the ideal qubit criteria in their ability for control and measurement, and scalability. But, it is the mechanisms that cause decoherence in the rf-SQUID qubit that are of greater importance for their utilization as a qubit in quantum computation applications.

The decoherence time of coherent quantum states in flux based superconducting qubits has inherent limitations related to the quality of the Josephson junction(s) in the qubit. Critical current fluctuations and the low-voltage subgap resistance of the junction(s) impose these limits through the Josephson energy and damping of the qubit[2, 3, 4]. These limits suggest that with a decay time from the excited qubit state of $\tau_{1/e} \sim 2$ μs at the operating temperature of the qubit having a Josephson junction with area of 4.5 μm^2, critical current of 2.25 μA and

a level spacing $\delta \sim 10^9$ s^{-1} between the coherent states, the normalized critical current fluctuations should be $S_{IcN}(1$ Hz$) \sim 10^{-22}$ (A^2/Hz)(μm/μA)^2 or less and the subgap resistance should be 10^9 Ω or greater.

The quasiparticle tunneling current (subgap leakage) and the low frequency critical current fluctuations in Josephson junctions fabricated at Stony Brook have been studied. The devices are fabricated from a Nb/AlO$_x$/Nb trilayer using a lift-off process and employing optical and electron beam lithography.

Subgap leakage measurements were performed down to 360 mK, and a subgap resistance greater than 1 GΩ is demonstrated. Low frequency current noise measurements of externally shunted junctions and unshunted junctions were acquired via a bridge circuit with a SQUID null current detector. Excess $1/f$ noise at low frequency was observed to decrease linearly from 4.2 K down to 410 mK, and the normalized critical current fluctuations measured at 1 Hz was $2.2 \cdot 10^{-24}$ A^2/Hz·(μm/μA)^2 at 4.2 K.

To Alex

Contents

List of Figures

List of Tables

Acknowledgements

Chapter 1

Theoretical Review

1.1 Introduction

The implementation of quantum computation processes such as fast database searches, fast factorization, and secure communications into the computational world is one of many goals in the continuing search for faster and faster processing speeds and the ultimate secure communications [5]. These quantum computational processes rely on the fundamental component of the so-called qubit. Realization of the qubit in a low-temperature solid state system such as the rf-SQUID holds the promise of attaining the desired qualities for the qubit [1]. The path to realizing the rf-SQUID as a qubit has involved characterization of its Josephson junctions in terms of properties that determine some of the limiting factors for the coherence of its quantum states.

Since the advancement of superconducting integrated circuit fabrication technology[6, 7, 8], various forms of superconducting qubits have been devised to study quantum mechanical coherence. Many of these forms of qubits have demonstrated quantum coherence via superposition of the quantum states, Rabi oscillations and Ramsey fringe measurements [9, 10, 11, 12, 13, 14, 15, 16]. Determining and resolving sources of decoherence in these qubits is an important issue in terms of general understanding of the superconducting qubit and in their development towards implementation as devices for quantum computation. Sources of noise external to the qubit can be minimized or eliminated[17, 18, 19], though inherent sources of decoherence in the qubit, its Josephson junction(s) and its co-fabricated environment, are likely the limiting factors to achieving coherence times adequate for quantum computation applications[1, 4].

The decoherence or dephasing time of flux based superconducting qubits has inherent limitations related to the quality of its Josephson junctions. The

critical current fluctuations and the low-voltage subgap conductance of the Josephson junction impose these limits through the Josephson energy and damping of the qubit [2, 3, 4]. These intrinsic limitations suggest that for a decay time from the excited state of $\tau_{1/e} \sim 2\ \mu$s at the operating temperature of the qubit having a Josephson junction with area of 4.5 μm^2, critical current of 2.25 μA and a level spacing $\delta \sim 10^9$ s^{-1} between the coherent states, the critical current fluctuations in the junction should be $S_{Ic}(1Hz) \sim 10^{-22}$A^2/Hz or less and the subgap resistance of the junction should be $10^9\ \Omega$ or greater. These design parameters require that careful fabrication techniques be implemented in order to produce Josephson junctions having those desired high quality characteristics.

Presently, a majority of the above mentioned qubits are fabricated using Al/AlO$_x$/Al shadow evaporation[9, 11, 12, 14, 16], a few Nb/AlO$_x$/Nb [10, 13] trilayers and NbN/AlN/NbN [20]. Al/AlO$_x$/Al shadow evaporation is a relatively simple fabrication technique[6] and produces high quality junction devices[21, 22]. Though, the longevity of those devices' high quality is well known to deteriorate over a relatively short time[23] due to the diffusion of oxygen into the aluminum. In addition, it is not currently possible to make large scale Al/AlO$_x$/Al Josephson junction circuits using the shadow evaporation technique. The fabrication of large scale Nb superconducting circuits is currently a well-established and reliable[8, 24] technology that is applied to the production of voltage standards, rf mixers for radio astronomy, RSFQ digital radio receivers, and ultra-low signal SQUID magnetometers. Therefore it is desirable to study material properties in the design of the rf-SQUID qubit from the viewpoint of qubit decoherence sources when deciding on the most viable configuration for qubit implementation.

Nb/AlO$_x$/Nb and Al/AlO$_x$/Al based Josephson junctions fabricated with reasonably low subgap leakage have been measured[21, 22, 25]. In addition, previous low frequency conductance and critical current measurements have shown low noise characteristics[26, 27, 28] with either a linear[28] or quadratic[27] temperature dependence down to millikelvin temperatures.

In light of these measurements, it is the goal of the work presented here to develop a system of measurements to characterize the junction quality parameters, which would give one the tools to relate the junction quality from the fabrication process to the decoherence properties in the qubits. In this chapter, the fundamental properties of superconducting Josephson junctions and the rf-SQUID are reviewed to introduce the system to be studied and to understand how the system is connected to rf-SQUID qubit quality [29]. Following the introduction, the fabrication process of the junction devices is discussed, then followed by the two junction quality measurements presented

here: the subgap quasiparticle transport and low-frequency critical current fluctuations in $Nb/AlO_x/Nb$ Josephson junctions. In the final chapter, closing arguments of the presented work and suggestions of future work will be discussed.

1.2 Josephson Junction Properties

1.2.1 Dynamics

The Josephson junction[30] is a superconducting tunneling device formed by a weak link between two superconducting materials and typically realized by an insulating barrier (junction) between the superconducting electrodes. The supercurrent can be described by a quantum mechanical wave function where the junction provides an interaction term in the form of the Josephson energy, $E(\phi) = E_J \cos\phi$, where $E_J = \hbar I_c/2e$ is the Josephson coupling energy. The consequence of the interaction is that a supercurrent (I_s) can flow across the junction with no dissipation (zero voltage) and has the form

$$I_s = I_c \sin(\phi). \tag{1.1}$$

where ϕ is the phase difference across the junction between the two superconductors, and I_c is the maximum supercurrent allowed without dissipation. If the phase difference is zero, the coupling energy is maximum ($E(0) = E_J$) and there is no current flowing through the junction. When the phase difference is nearly $\pi/2$, the Josephson energy is nearly 0 and the maximum supercurrent flows through the junction. Above the maximum supercurrent the phase difference across the junction begins to evolve in time according to

$$\frac{d\phi}{dt} = \left(\frac{2e}{\hbar}\right)V \tag{1.2}$$

so that an average voltage, V, develops across the junction and an ac current flows with frequency

$$f = \left(\frac{2e}{h}\right)V = \frac{V}{\Phi_o}, \tag{1.3}$$

where e is the elementary charge, $\hbar = h/2\pi$ (h is Planck's constant), and Φ_o is the flux quantum ($\Phi_o^{-1} \cong 483.6$ MHz/μV).

The current-voltage characteristics of a biased Josephson junction can be adequately described in most cases by the RSJ (resistively shunted junction) circuit model. The junction is broken down into parallel components of an ideal junction, a capacitance, C, and a shunting resistor, R as shown in Fig.
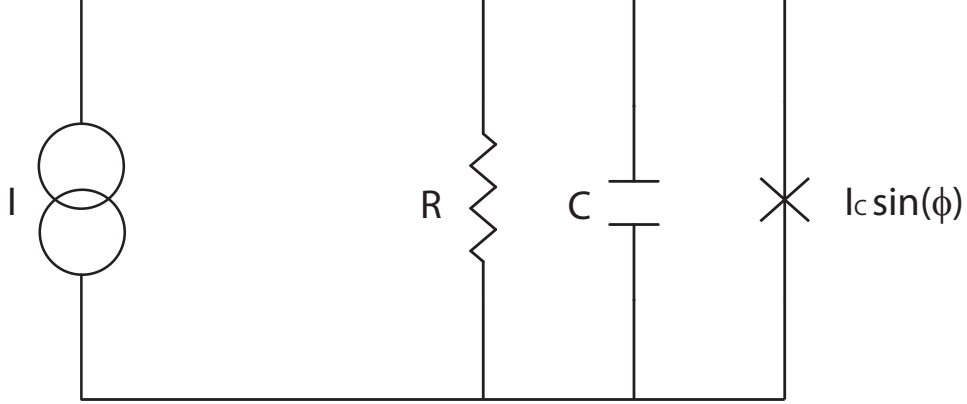
Figure 1.1: Diagram of the equivalent circuit for a current biased Josephson junction.

1.1. The total current through the junction is then written as

$$I = I_c \sin(\phi) + \frac{V}{R} + C\frac{dV}{dt}, \tag{1.4}$$

which can be rewritten as an equation of motion for the phase

$$\frac{d^2\phi}{d\tau^2} + \frac{1}{\beta_c^{1/2}}\frac{d\phi}{d\tau} + \sin(\phi) = \frac{I}{I_c}. \tag{1.5}$$

$\beta_c = (\omega_p RC)^2$ is the damping parameter[31, 32] of the junction and $\tau = \omega_p t$, where $\omega_p = [2eI_c/(\hbar C)]^{1/2}$ is the plasma frequency of small oscillations of the phase in the "washboard" potential of the Josephson junction

$$U(\phi) = -E_J\left(\cos(\phi) + \frac{I}{I_c}\phi\right). \tag{1.6}$$

Overdamped Junctions

When the ideal junction is shunted by an external resistor, R_{sh}, such that $\beta_c < 1$, and in the limit of small capacitance $(C \to 0)$ and zero temperature, the RSCJ model, Eqn. 1.5, reduces to a first-order differential equation, which can be solved to give the voltage-current expression

$$V(I) = R_{sh}\left(I^2 - I_c^2\right)^{1/2}. \tag{1.7}$$

For $I < I_c$, $V = 0$. For $I \gg I_c$, $V \to IR_{sh}$.

4

Real junctions, though, are affected by thermal fluctuations at finite temperatures. This scenario was investigated by Ivanchenko and Zil'berman[33] and Ambegaokar and Halperin[34]. The authors included a current noise term, $\tilde{I}(t)$, in the RCSJ model having a Nyquist spectral density, $S_I(f) = \frac{4k_B T}{R_{sh}}$, which is uncorrelated and its time averaged mean value is zero. They found in the zero capacitance limit that the voltage-current expression is modified by a finite temperature and is found to be

$$V(I) = \frac{2R_{sh}I_c}{\gamma} \left(\frac{e^{\pi\gamma\alpha} - 1}{e^{\pi\gamma\alpha}} \right) T_1^{-1} \tag{1.8}$$

where

$$T_1 = \int_0^{2\pi} \exp\left(-\frac{\gamma}{2}\alpha\phi\right) I_o\left(-\frac{\gamma}{2}\alpha\phi\right) d\phi \tag{1.9}$$

and $\gamma = I_c\Phi_o/\pi k_B T$, $\alpha = I/I_c$. The effect is a bending in the I-V characteristic near the critical current as shown in Fig. 1.2 where Eqn. 1.7 is also shown for comparison. This effective decrease in the critical current is due to the phase across the junction randomly slipping and trapping while biased nearly at the $T = 0$ critical current value.

Underdamped Junctions

When $\beta_c > 1$ the junction I-V becomes hysteretic as shown in Fig. 1.3. Upon passing I through I_c a voltage develops across the junction equivalent to the gap voltage, $V_g = 2\Delta/e$ for $T \ll T_c$. Increasing the current, the junction follows the quasiparticle step at the gap voltage until $I \approx V_g/R_N$, where R_N is the normal resistance of the junction. The junction then follows Ohms law ($V = IR_N$), for $I \gg I_c$, with increased current.

After the junction switches out to the gap voltage to its "running" state, if the current is decreased, the voltage remains at the gap voltage until $I \simeq V/R_{sg}$, where R_{sg} is the quasiparticle tunneling resistance in the subgap. The junction roughly follows $V \approx IR_{sg}$ until the current reaches the retrapping current value, I_r, at which point the voltage drops to zero and back into the "trapped" supercurrent state. In zero magnetic field the retrapping current is roughly given by $I_r \approx 4I_c/\pi\beta_c^2$. Typically, β_c is of the order of 100 or larger for high quality junctions[35] meaning that $I_r \lesssim I_c \cdot 10^{-4}$.

1.2.2   Quasiparticle Transport

The quasiparticle current-voltage characteristics of the underdamped junction is described by pair breaking (injecting an electron into one electrode
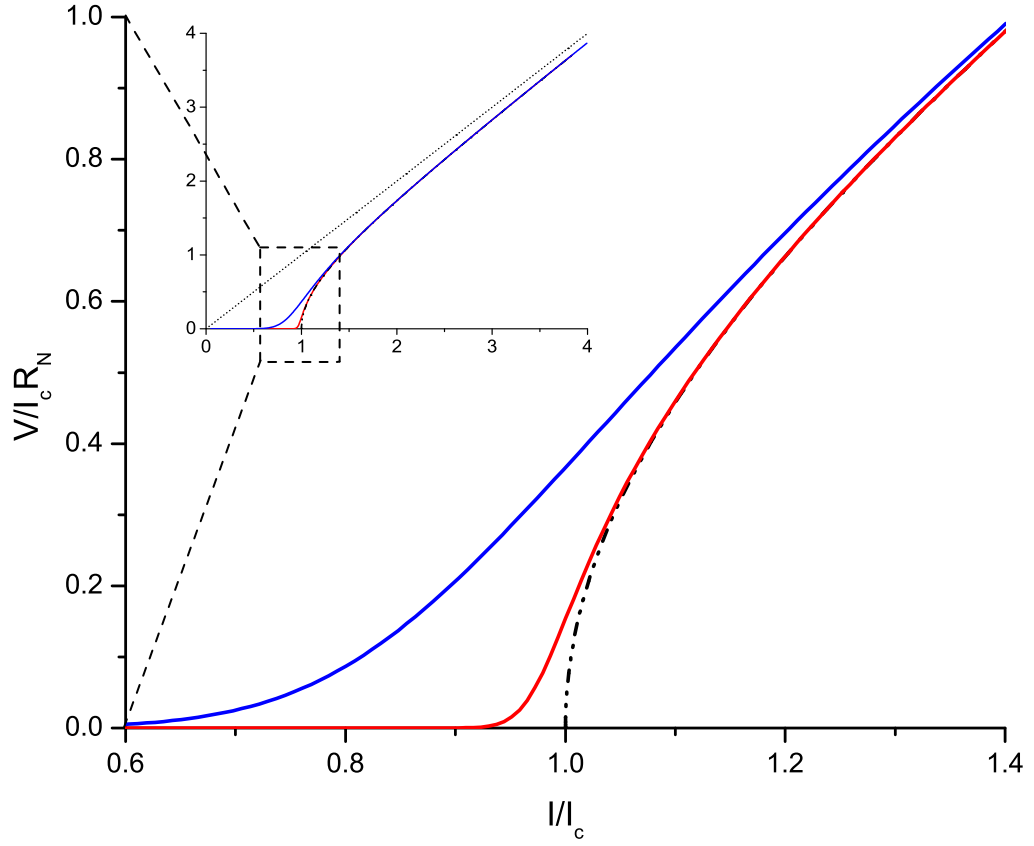
Figure 1.2: Voltage-current characteristic curves of an externally shunted Josephson junction for $T = 0$ (black dashed line) and finite T. $T = 4.2$ K, $\beta_c = 0.27$, $\gamma = 280$ (red) and 20 (blue). The dotted line in the inset is equivalent to the normalized shunt resistance. The scales are normalized units of voltage and current.
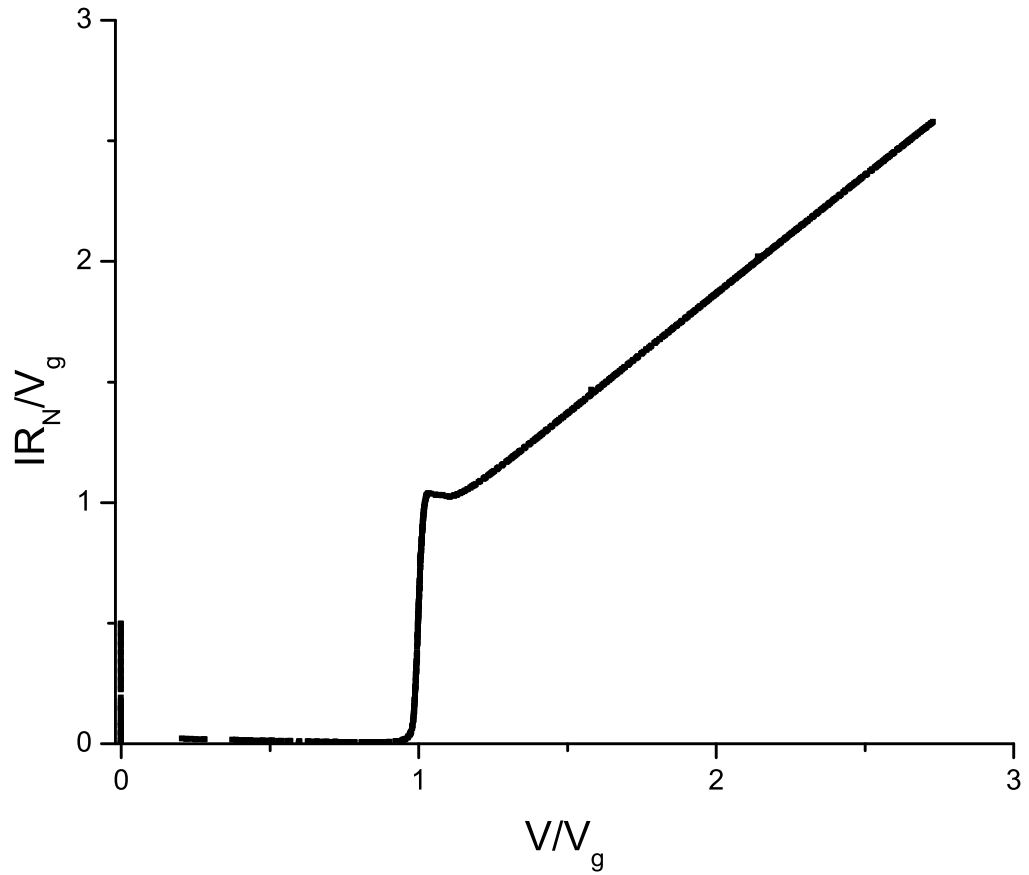
Figure 1.3: Data of a normalized current-voltage characteristic for an unshunted Josephson junction at $T = 4.2$ K. The scales are in units of the gap voltage, V_g, and the ratio of the gap voltage to the normal resistance, V_g/R_N.

and creating a hole excitation in the other) and the tunneling of excited electrons. The total BCS tunneling quasiparticle current, I_{qp}, is calculated as an integral over the density of states of the two superconducting electrodes, their fermi distributions and tunneling matrix given by

$$I_{qp} = \frac{1}{eR_N} \int_{-\infty}^{\infty} \frac{|E' - eV|}{\left[(eV - E')^2 - \Delta^2\right]^{1/2}} \frac{|E'|}{\left[E'^2 - \Delta^2\right]^{1/2}} \left[f(E' - eV) - f(E')\right] dE'.$$
(1.10)

In the limit $T \ll \Delta/k_B$ and small voltages ($eV < 2\Delta$), the quasiparticle tunneling current can be approximated by

$$I_{qp} = \frac{2}{eR_N} e^{-\Delta/k_B T} \left(\frac{2\Delta}{eV + 2\Delta}\right)^{1/2} (eV + \Delta) \sinh\left(\frac{eV}{2k_B T}\right) K_o\left(\frac{eV}{2k_B T}\right).$$
(1.11)

K_o is the zeroth-order modified Bessel function. This indicates that there is always a finite amount of tunneling quasiparticles at low bias voltages ($V \ll V_g$) that is exponentially dependent upon the junction temperature. High quality Josephson junction devices are typically those that have quasiparticle current levels at low voltage that are comparable to the BCS expression in Eqn. 1.11.

1.2.3 Effect of Magnetic Fields

A superconductor in the presence of a magnetic field will generate a screening current due to the Meissner effect in order to expel the magnetic field. The penetration depth, λ, is the length scale in which the external magnetic field is reduced by 1/e from the edge of the superconductor. In thin-film Josephson junctions, the physical oxide barrier is only a few Ångstroms thick, where the penetration depth is on the order of ~ 1000 Ångstroms, therefore, in magnetic fields, the junction thickness is determined by the penetration depth, λ.

The Josephson supercurrent, in the presence of a magnetic field, becomes modulated by the field threading through the "normal" region of the junction as illustrated in Fig. 1.4. The current density in the junction along the length of a uniform square junction is found to be

$$J(z) = J_c(z) \sin\left[\left(\frac{2edB}{\hbar}\right) z + \phi(0)\right]$$
(1.12)

where z follows along the length of the junction, $\phi(0)$ is a constant of integration that takes the value $\pm\pi/2$ at the maximum of the critical current,

(a)

$\Phi = 0$

(b)

$\Phi = 1/2 \ \Phi_o$

(c)

$\Phi = \Phi_o$

(d)

$\Phi = 3/2 \ \Phi_o$
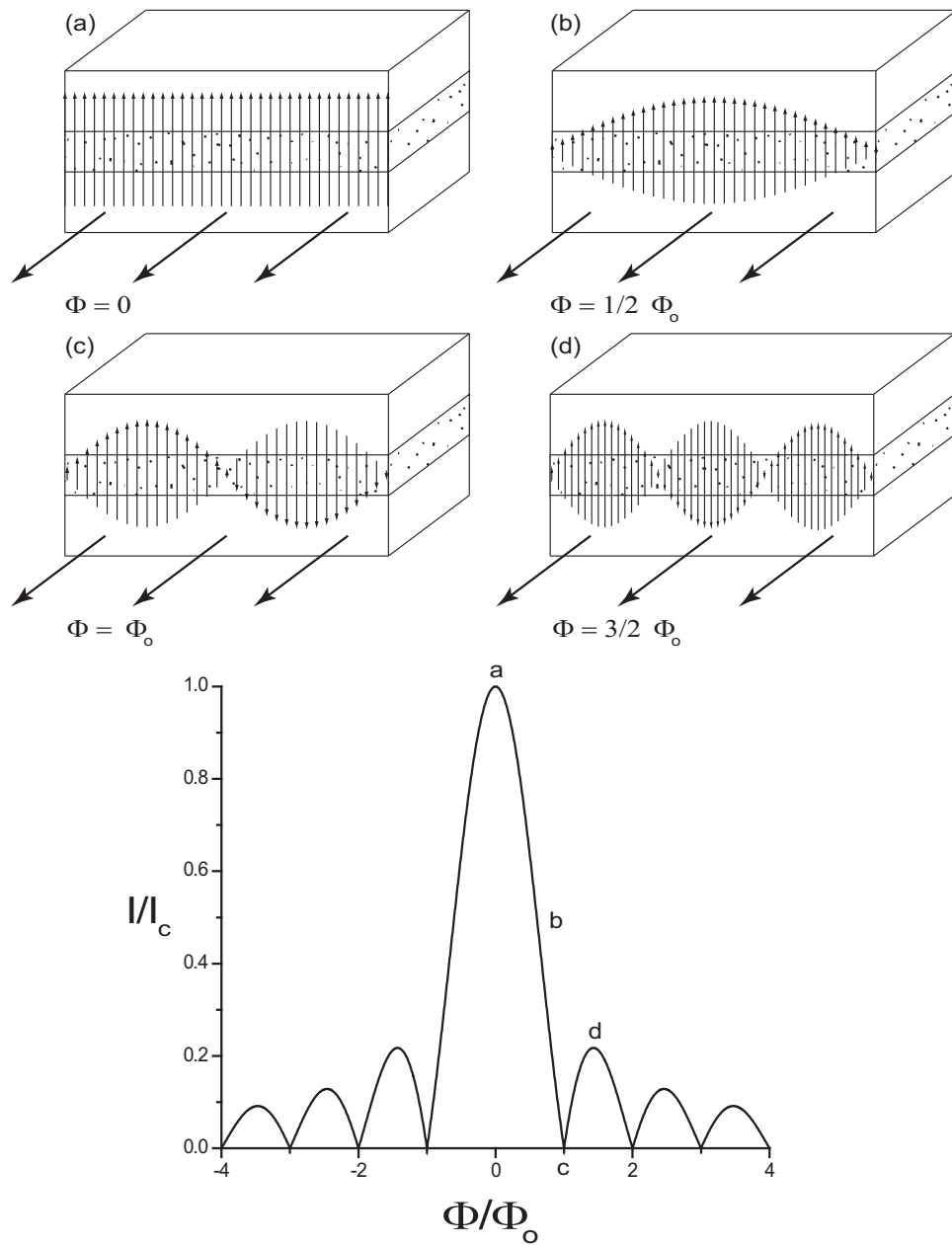
Figure 1.4: Illustration of the spatial modulation of the current density in a uniform junction for magnetic flux values of (a) 0, (b) $1/2\Phi_o$, (c) Φ_o and (d) $3/2\Phi_o$. Corresponding critical current modulation with magnetic flux.

9

$d \sim 2\lambda$ is the junction thickness seen by the magnetic field, B is the magnetic field strength, and $J_c(z)$ is the critical current density along the junction length, L.

Assuming a uniform critical current density and a square junction with area $A = L^2$, the dependence of critical current on the magnetic field, B, is found to be

$$I_c(\Phi) = I_c(0) \left| \frac{\sin(\pi\Phi/\Phi_o)}{(\pi\Phi/\Phi_o)} \right|, \tag{1.13}$$

which is expressed in terms of the total flux through the junction, $\Phi = dLB$, and $I_c(0)$ is the zero magnetic field critical current.

1.2.4 Electronic Fluctuations

The subject of electronic noise in devices has been extensively studied since Johnson's first measurements of voltage fluctuations in metallic resistors [36]. The impetus usually being that the electronic noise in a device determines the dynamic range, or resolution, of the device. That is, the sensitivity to detect changes in a signal measured in the device, say voltage, is ultimately limited by the inherent level of electronic noise in the device.

Johnson/Nyquist Noise

Fluctuations of the charge carriers at thermal equilibrium in a metallic device, such a resistor, lead to voltage fluctuations across the device. Nyquist modeled the behavior[37] discussing that for thermal equilibrium to hold for two resistors connected in parallel, the power transferred between them, due to the fluctuations, over a frequency interval $d\nu$, should take the form

$$V_n^2 d\nu = 4Rk_BT d\nu \tag{1.14}$$

where V_n is the RMS voltage per unit $\sqrt{\text{Hz}}$ across the resistor due the the fluctuations, k_B is the Boltzmann constant, R is the device resistance, and T is the temperature. The voltage noise per unit bandwidth of the resistor is then written as

$$V_n = \sqrt{4Rk_BT}, \tag{1.15}$$

The equivalent circuit for a noisy resistor, $\tilde{R}$, shown in figure 1.5a, is its Johnson noise source, V_n, and an ideal noise-free resistor, R, in series.

Alternatively, the Johnson noise source can be viewed as a current noise
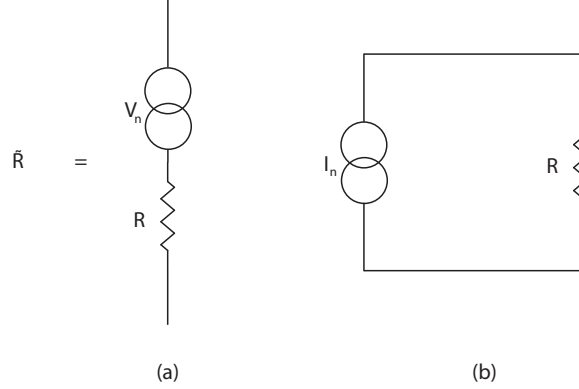
Figure 1.5: Circuit diagrams showing voltage and current noise equivalents representing thermal equilibrium Johnson noise in a resistor.

source by rewriting Eqn. 1.15 as

$$I_n = \frac{V_n}{R} = \sqrt{\frac{4k_BT}{R}}.$$ (1.16)

The equivalent circuit for the noisy resistor, $\tilde{R}$, is then the Johnson current noise source, I_n, in parallel with a noise-free resistor, R, as shown in Fig. 1.5b.

Fluctuations in the Josephson Junction

When voltage is present across a resistively shunted Josephson junction an ac current is generated according to Eqn. 1.4. Fluctuations in the voltage across the junction due to thermal fluctuations in turn generates a broad spectrum of current fluctuations, and the two are related by, $S_V = R_D^2 S_I$, where R_D is the dynamic resistance at the bias point of the junction. These fluctuations in the Josephson junction are evident from the rounding of the I-V characteristic, as seen in Fig. 1.2, and in the linewidth of the radiation at the Josephson frequency $f_J = 2eV/h$. The Josephson frequency radiation is also observed as mixed-down excess "white" noise in low frequency spectral measurements[38].

For low frequencies, $f \ll f_J$, and for current bias larger than the critical current ($I/I_c > 1$) the current fluctuations in the Josephson junction take the form [38, 39]

$$S_I = \frac{4k_BT}{R} + \frac{2eV}{R} \coth\left(\frac{eV}{k_BT}\right).$$ (1.17)

The first term on the left is the Johnson noise of the shunting resistor at low

11

frequencies compared to the Josephson frequency, $f_J = 2eV/h$. The second term is the current noise from fluctuations at the Josephson frequency, f_J, mixed down by the junction to low frequencies. In the limit of low voltage, where $V \ll k_B T/e$, the current noise reduces to the Johnson noise (thermal equilibrium fluctuations) of the junction shunt resistance, R, and the noise mixed-down from the Josephson frequency

$$S_I = \frac{4k_B T}{R} \left[1 + \frac{1}{2} \left(\frac{I_c}{I} \right)^2 \right]. \tag{1.18}$$

The above expressions are not accurate[38, 40] near I_c in the noise rounded region of the junction I-V due to the deviation of V from the zero capacitance relation (Eqn. 1.7).

In addition to thermal equilibrium and non-equilibrium current fluctuations in the Josephson junction, there are also fluctuations in the critical current, S_{Ic}, due to fluctuations in the barrier potential of the junction. These fluctuations in the critical current in turn cause fluctuations in the current, which is proportional to the voltage fluctuations of the junction and its dynamic resistance, R_D. The prevalent model of critical current noise is that charge traps in the tunnel barrier[41, 42] are the source of the fluctuating critical current. Due to Coulomb repulsion the tunneling supercurrent is blocked in the vicinity of the trapped charge. This effectively reduces the tunneling area and therefore modulates the critical current.

The trapping and untrapping rates of the charge trap together have an effective rate $\tau_{\mathrm{eff}} = (1/\tau_{\mathrm{t}} + 1/\tau_{\mathrm{u}})^{-1}$ that defines a Lorentzian spectrum[41, 43] having the form

$$S_{trap,i}(f) = S_i \frac{\tau_{\mathrm{eff},i}}{1 + (2\pi f \tau_{\mathrm{eff},i})^2}. \tag{1.19}$$

A large randomly distributed ensemble, N, of such traps in a junction of area, A, having a uniform distribution of trap rates produces a $1/f$-like spectrum, which is a characteristic low-frequency excess noise observed in Josephson junctions.

When the charge trap is momentarily filled, the change in the critical current is proportional to a change in the effective tunnel area of the junction given by[4] $\Delta I_c = (\Delta A/A) I_c$. The spectral density of critical current fluctuations, $S_{Ic}(f)$, is then proportional to $N(\Delta I_c)^2 = nA (\Delta A/A)^2 I_c^2$, where $n = N/A$ is the number of charge traps per unit area in the junction. It is then expected that the critical current fluctuations at 1 Hz for a given temperature, T, should scale as

$$S_{Ic}(T) \approx S_{IcN}(T) \frac{I_c^2}{A}. \tag{1.20}$$

The value $S_{IcN}(T)$ is a quantity that characterizes the number of fluctuators per unit area, n, in the junction barrier for a given temperature and should be independent of junction size and critical current density.

1.2.5   Superconducting rf-SQUID Qubit

A superconducting loop interrupted by a Josephson junction as shown in Fig. 1.6 has two macroscopic variables: the flux penetrating the loop and any circulating current in the loop. The junction creates interference with the loop's own superconducting wavefunction and modifies the quantization of flux in the loop. The phase difference, ϕ, across the junction in the loop is found to be

$$\phi = 2n\pi - \frac{2\pi\Phi}{\Phi_o} \tag{1.21}$$

where Φ is the total flux in the superconducting loop. If one applies an external flux, at equilibrium the total flux in the loop becomes the sum of the applied flux and the induced current in the loop given by

$$\Phi = \Phi_x + LI \tag{1.22}$$

where L is the superconducting loop inductance and I is the induced equilibrium current in the loop. The Josephson current relation (Eqn. 1.1) with Eqn. 1.21 included gives the induced current in the loop as an implicit relation

$$I = -I_c \sin\left\{ \frac{2\pi\Phi}{\Phi_o} + \beta_L \frac{I}{I_c} \right\} \tag{1.23}$$

where I_c is the maximum critical current, and $\beta_L = 2\pi L I_c/\Phi_o$. We can rearrange Eqn. 1.23 to find an implicit relation between the total flux and applied external flux at equilibrium to be

$$\frac{\Phi}{\Phi_o} = \frac{\Phi_x}{\Phi_o} - \frac{\beta_L}{2\pi} \sin\left(\frac{2\pi\Phi}{\Phi_o} \right). \tag{1.24}$$

For $\beta_L > 1$ the path that the total flux, Φ, follows at equilibrium as a function of the applied external flux, Φ_x, is hysteretic as indicated in fig. 1.7. The hysteretic path may be illustrated if one examines the general equation of motion for an rf-SQUID and its energy potential

$$C\ddot{\Phi} + \frac{\dot{\Phi}}{R} = -\frac{\partial U\left(\Phi, \Phi_x\right)}{\partial \Phi} \tag{1.25}$$

13
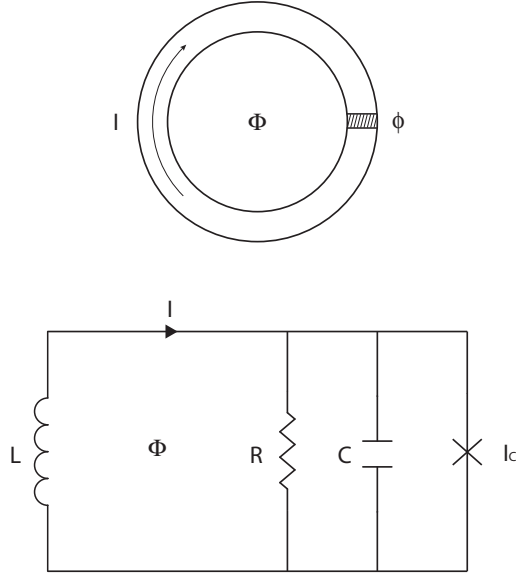
Figure 1.6: Diagram of an isolated rf-SQUID and its equivalent circuit.

$$U\left(\Phi, \Phi_x\right) = U_o \left[\frac{1}{2} \left(\frac{\Phi - \Phi_x}{\Phi_o}\right)^2 + \beta_L \cos\left(2\pi \frac{\Phi}{\Phi_o}\right)\right], \qquad (1.26)$$

where $U_o = \Phi_o^2/4\pi^2 L$, and imagines that the average flux of the system at equilibrium is described by a particle with mass C (the junction capacitance) lying in one of the wells of the potential and has a damping term, R^{-1}, given by the junction shunt resistance.

At $T = 0$, as the external flux is applied, the potential tilts and the average total flux gradually changes until the well that the particle is in disappears and the particle falls into the adjacent well, lowering its total energy, and abruptly transitions to another average flux value, which is roughly equivalent to a flux quantum. This sequence is shown in Fig. 1.8. At finite temperatures above the thermal activation regime $(T > T_o = \hbar\omega_T/k_B)$[44, 45], the particle (or flux state) can pass over the barrier before it disappears. The attempt rate of passing over the barrier follows an Arrhenius law

$$\Gamma = \frac{\omega_T}{2\pi} e^{-\Delta U/k_B T}, \qquad (1.27)$$

where ω_T is the thermal attempt frequency of the particle in the well and is related to the plasma frequency and damping of the circuit. ΔU is the barrier height measured from the well minimum to the lowest first maximum and is a function of the applied external flux to the SQUID.

14
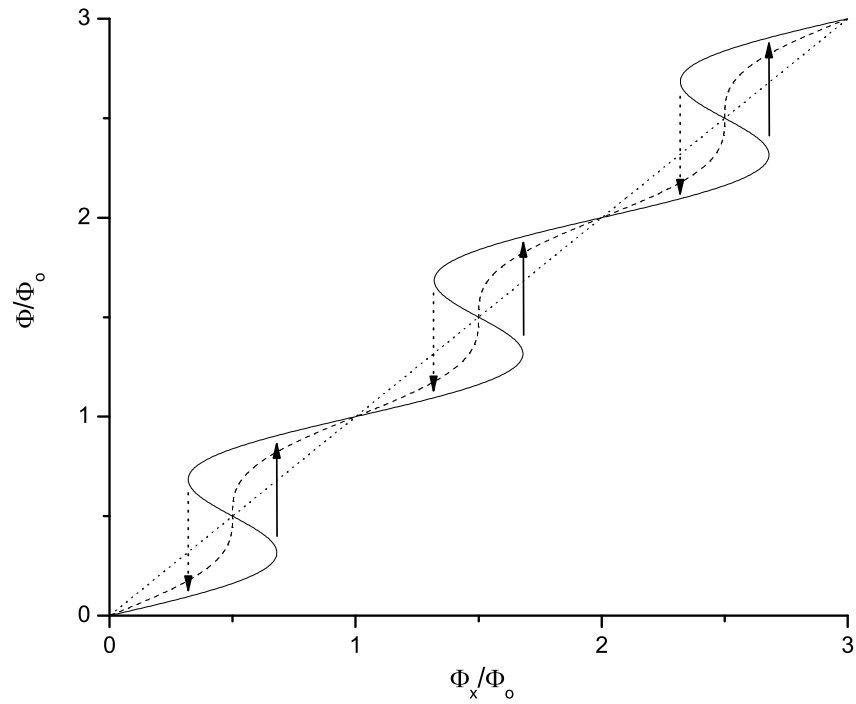
Figure 1.7: Dependence of the total flux in an rf-SQUID with applied external flux, Φ_x, for $\beta_L = 2.5$ (solid), 1 (dashed), and 0 (dotted). Solid and dashed arrows indicate flux transitions on the $\beta_L = 2.5$ curve for, respectively, increasing and decreasing Φ_x.
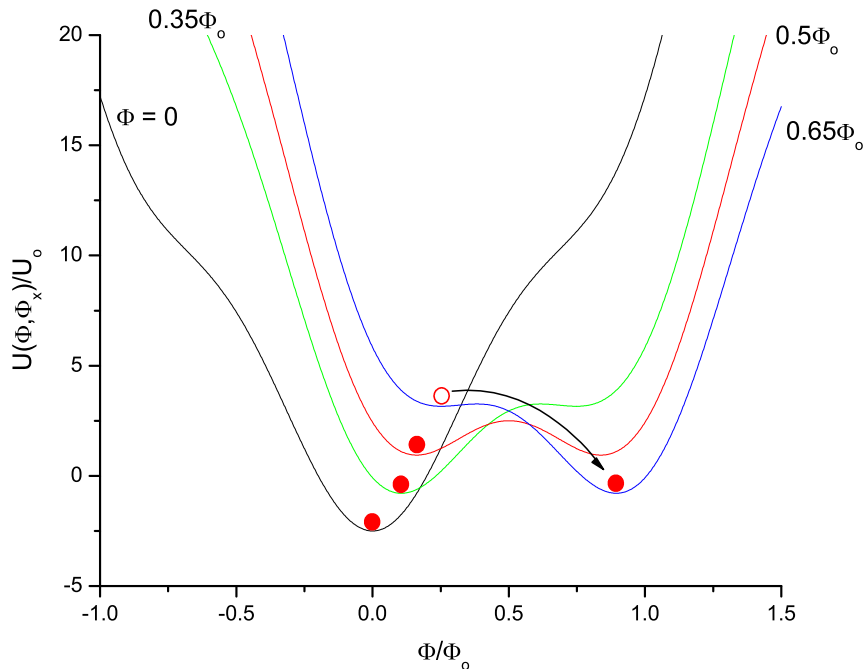
Figure 1.8: The rf-SQUID potential showing a sequence of applied external flux, Φ_x, for $\beta_L = 2.5$. The solid circle in the well of each curve represents the average flux value at the indicated applied flux.

For temperatures much less than T_o, tunneling rather than thermal activation begins to dominate the dynamics of the system [45]. The tunneling dynamics and the associated damping is of interest due to its importance in the context of quantum computation. The rf-SQUID can be utilized as a qubit in at least two distinct ways using the quantized energy states: as a phase qubit or flux qubit when $E_J \gg E_c$, where $E_c = e^2/2C$ is the Coulomb charging energy.

In the phase basis, the qubit states are the ground state, $|0\rangle$, and first excited state, $|1\rangle$, having the same flux state, say $|L\rangle$, in the rf-SQUID. The state of the qubit is measured by rapidly changing the flux through the rf-SQUID so that escape from the excited state, $|1\rangle$, to the adjacent flux state, $|R\rangle$, is much more likely than the escape of the ground state, $|0\rangle$, to the adjacent flux state [29]. Then, this measurement is repeated to accumulate statistics of the qubit state for a given Φ_x bias. If the system was in the ground state, the escape rate for tunneling into an adjacent well (to another

flux state) is small and very few tunneling events are recorded. If the system was in the excited state, the escape rate for tunneling is approximately 2 orders of magnitude larger making a tunneling event very likely [29].

In the flux basis scheme, the rf-SQUID is biased with an applied external flux such that the two lowest energy levels, $|L\rangle$ and $|R\rangle$, in adjacent wells are degenerate, which occurs at $\Phi_x = \Phi_o/2$, as seen in Fig. 1.9. For small enough energy barrier, which is determined by β_L, separating the two wells and T being below the particular crossover temperature for this system (T less than the energy level spacing), the coupling between the two localized states then leads to an energy level splitting in the diagonalized basis of the coupled flux states. By preparing the state of the system to be in one well by biasing Φ_x far from resonance, then rapidly moving the potential to resonance at $\Phi_x = \Phi_o/2$, oscillations of the flux between the two wells will occur at a frequency equivalent to the energy level splitting. Determination of the state of the system is implemented by simply measuring the flux in the rf-SQUID.

1.3 Sources of Decoherence in an rf-SQUID Qubit

1.3.1 Quasiparticle Damping

Ideally, the superconducting rf-SQUID qubit could be well isolated from any environmental interaction. Though, dissipation of the coherent state of the qubit can be an intrinsic property of its own making. In an ideal Josephson junction at zero temperature, tunneling quasiparticles are allowed only at a potential bias across the tunnel barrier that is equivalent to twice the superconducting energy gap ($V_g = 2\Delta/e$). At finite temperatures we see from Eqn. 1.11 that a small amount of quasiparticles can tunnel across the barrier at voltage less than V_g. This is a mechanism for dissipation in the rf-SQUID, which can be illustrated as a shunt resistor, R, across the junction, as in Fig. 1.1.

Assuming the qubit state has been properly prepared, the rf-SQUID potential biased such that it is a symmetric double well potential, and temperatures are well below the thermal activation regime, T_o, the qubit state can tunnel coherently, oscillating between the two flux states of the rf-SQUID potential. With Ohmic dissipation the oscillations become damped where the amplitude of the system state is described by[2, 3]

$$P_L = \frac{\cos\left(\delta t - \phi\right)}{\cos\left(\phi\right)}e^{-\gamma t}, \tag{1.28}$$

17

where

$$\gamma = \frac{\phi_m^2 \delta}{4R\hbar} \tag{1.29}$$

is the relaxation rate with a tunnel splitting frequency, or oscillation frequency, δ, and ϕ_m is the separation in flux between the two well minima. The phase difference is given by

$$\phi = \tan^{-1}\left(\frac{\gamma}{\delta}\right), \tag{1.30}$$

which can be made small for γ much smaller than δ, meaning long coherence times. For the qubit system to have a large ratio of the oscillation rate, δ, to relaxation rate, γ, or Q, on the order of 10^6 - meaning a large number of coherent oscillations before the system state amplitude decoheres by $1/e$ - implies that the shunt resistance, or resistance in subgap quasiparticle regime, at the qubit operation temperature and at the tunnel splitting frequency should be on the order of $R(\delta) \gtrsim 10^9 \ \Omega$. The ratio of the resistance in the subgap quasiparticle regime to the normal resistance, $R(\delta)/R_N$, is a convenient normalizing parameter that closely follows Q. This parameter will be used in the discussion of results in chapter 3.

1.3.2   Low-Frequency Noise

Intrinsic sources of noise in the rf-SQUID are charge noise, flux noise, and critical current noise. In the system referred to here, $E_J \gg E_c$, so that charge noise is considered negligible. Flux noise from flux pinning in the superconducting circuit lines of the rf-SQUID can be made negligible[46] by designing the SQUID to have narrow lines less than $(\Phi_o/B)^{1/2}$, where B is the ambient magnetic field. The ambient field can be suppressed by proper shielding to the order of 10^{-3} Gauss so that designed circuit linewidths of 100 μm or less are adequate. In addition, designing the rf-SQUID in a gradiometer configuration reduces first order flux noise extrinsic to the rf-SQUID.

Critical current noise is perceived to be of greater concern because it is a limiting source of decoherence in the rf-SQUID qubit. As mentioned above, the prevalent model of critical current noise is that it is caused by charge traps in the tunnel barrier[41, 42]. In the flux basis scheme of the qubit, fluctuations in the critical current lead to fluctuations in the energy level splitting of an rf-SQUID qubit biased at its degeneracy point. The energy level splitting between the ground and first excited energy levels of the coupled flux states is exponentially dependent on the critical current[47]

$$\delta \approx \omega_o exp\left[-\eta\left(\beta_L - 1\right)^{3/2}\right], \tag{1.31}$$
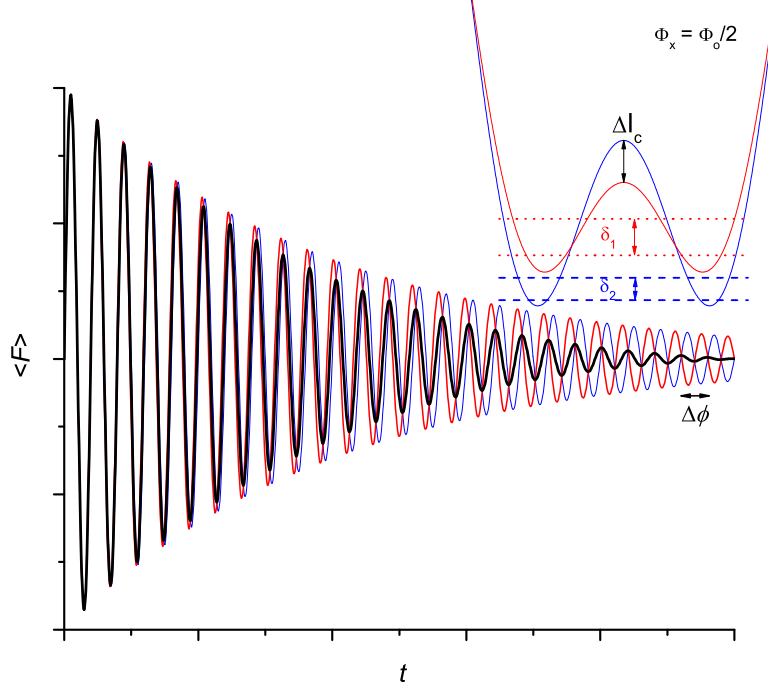
Figure 1.9: Coherent oscillations of the flux state $\langle F \rangle$ of the rf-SQUID qubit when the potential is flux biased to $\Phi_o/2$ (inset). The thick black oscillation curve shows the effective decrease in the qubit state obtained from time averaging over many measurements. The inset depicts two representative energy potentials and the associated energy level splitting of the coupled flux states.

where, ω_o, is the plasma frequency, $\eta = \left(8I_cC\Phi_o^3/\pi^3\hbar^2\right)^{1/2}$ and $\beta_L = 2\pi LI_o/\Phi_o$.

Fluctuations in the energy level splitting, δ, leads to phase noise in the qubit due to the measurement process of determining the qubit state. At any particular time the qubit state amplitude is determined by averaging over many measurements of the qubit state amplitude. Figure 1.9 illustrates the how critical fluctuations, ΔI_c, in the rf-SQUID qubit induces phase noise, $\Delta\phi$, between successive measurements of the qubit state. Over the course of those many measurements to determine the qubit state where δ has been fluctuating, the phase of qubit state amplitude from one measurement to another fluctuates therefore effectively inducing decoherence when the measurements are averaged together.

Chapter 2

Fabrication and Characterization of Josephson Junctions

2.1 Self-aligned Lift-off and Electron Beam Lithography Process

The shunted and unshunted Josephson junction devices were fabricated using the Stony Brook SAL-EBL process [35, 48]. The process yields high quality deep-submicron junctions with dimensions as small as 0.15 x 0.15 μm^2. The reliable uniformity of the junction area allow us to accurately design a desired junction size. The junctions fabricated for this work ranged in size on our diagnostic chips from 0.15 x 0.15 μm^2 to 9.8 x 9.8 μm^2. Subgap current measurements were performed on junctions sizes of 1.4, 1.8, 4.8, and 9.8 μm, while critical current fluctuation measurements were performed on 1.5, 2, 5 and 10 μm size junctions.

The first step in the Self-aligned Lift-off (SAL) process is the patterning of the Nb/AlO$_x$/Nb trilayer via lift-off. This step reduces the number of reactive ion etches (RIE) in the process and minimizes damage to the Nb[49]. This first step begins with a 50 mm oxidized Si wafer being coated with a PMMA/P(MMA/MAA) bilayer resist that is patterned by UV lithography and by electron beam lithography (EBL). The trilayer is then deposited by DC magnetron sputtering in a cryopumped vacuum system at base pressures around 10^{-7} Torr. The Nb base (BE) and counter (CE) electrodes are typically 150 nm thick and the Al interlayer is 8-10 nm thick. The oxide barrier is formed by thermal oxidation in a static atmosphere of dry O$_2$. A total O$_2$ exposure of 103-104 Torr-min gives current densities, J_C, of 50-150 A/cm^2. The completed

trilayer deposition step is shown in Fig. 2.1a and Fig. 2.1b-g illustrates the remaining process steps. After the trilayer deposition the wafer is soaked in a bath of acetone for at least 6 hours, then in a stripper solution and finally cycled through an oxygen plasma asher to clean off any remnant resist (Fig. 2.1b).

The junctions (CE) are patterned using a Shipley Inc. UVN-30 resist after the trilayer lift-off. UVN-30 is a deep UV resist which our group has developed for negative tone and EBL [48]. The achieved resist resolution is better than 100 nm. The junctions are defined by RIE in SF_6 plasma. Etch end-point detection is achieved by monitoring the Fluorine optical emission spectra during the RIE. The UVN-30 is a not an erodable resist in the SF_6 plasma, therefore there is a measurable undercut of the etched Nb pedestal (CE) (Fig. 2.1c). This undercut is uniform and the junctions remain square down to sub-micron sizes. This allows for determination of the amount of undercut from the observed electrical characteristics of the junctions and calibrate our etch process to allow the design of junctions into the deep sub-micron sizes.

After the RIE, a 160-170 nm SiO_2 dielectric is RF sputtered on to the wafer. The UVN-30 resist is then stripped exposing the Nb CEs thus completing the self-aligned lift-off (Fig. 2.1d). The RF sputtered SiO_2 has good sidewall coverage and seals the junctions well, preventing shorts between the wiring and BE around the junction.

Contact holes are initially defined as junctions and are subsequently formed by SF_6 RIE of the CE followed by an Al wet etch (Fig. 2.1e). Next the resistors are defined by lift-off of e-beam evaporated AuPd (Fig. 2.1f). Finally a 250 nm thick Nb wiring layer is formed, again by lift-off (Fig. 2.1g). The entire SAL-EBL process takes about 5 days to finish.

2.2   Characterization of SAL-EBL Junctions

Standard junction test chips contain 62 square junctions with design areas ranging from 0.09 μm^2 to 100 μm^2. Scaling statistics of the junctions' electrical properties are gathered from measuring individual junctions rather than junction arrays. The test chips with junctions are wire bonded to a 62 lead chip carrier and inserted into an IC socket mounted at the end of a custom made vacuum-tight cryostat for dipping into liquid helium. The wiring of the probe from room temperature to the IC socket is provided by high resistance wire leads having about 15 Ω/ft and are thermally anchored at 4.2 K.
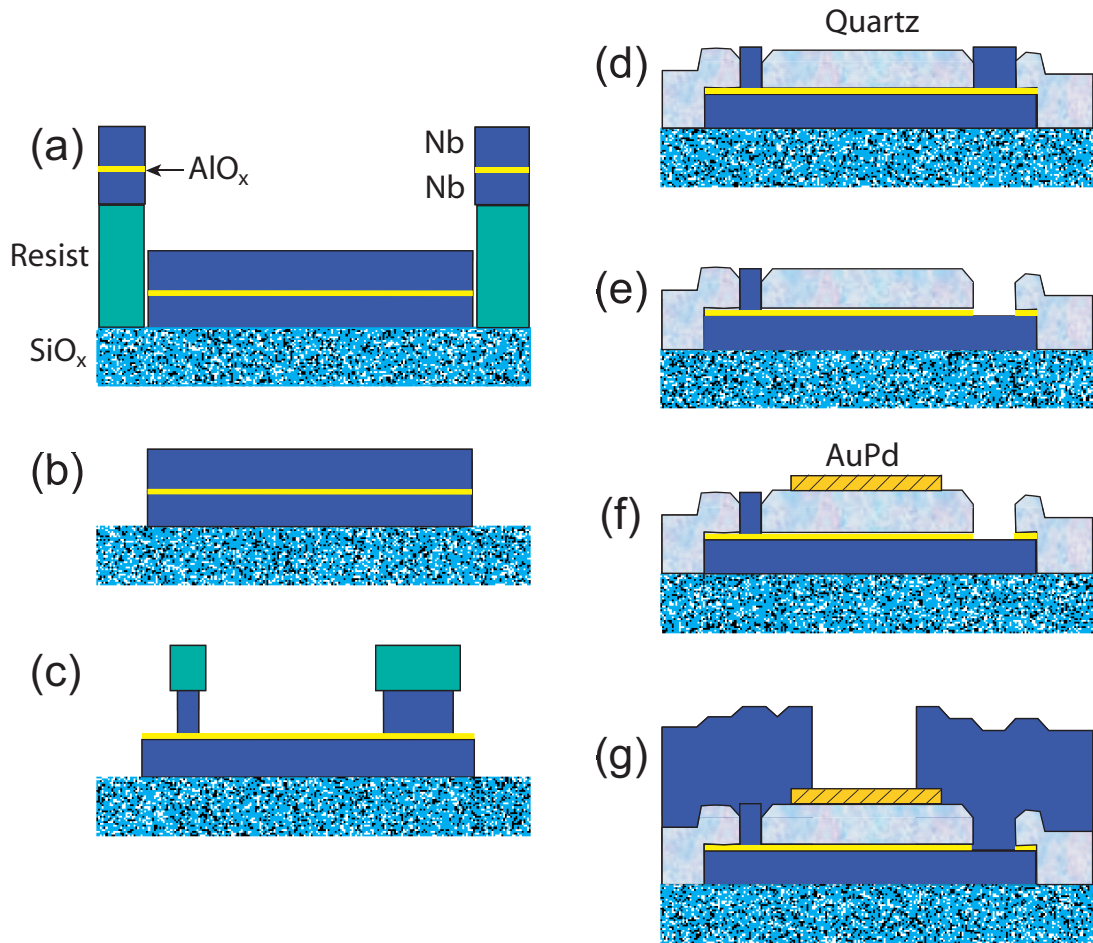
Figure 2.1: Illustration of SAL-EBL process. (a) Trilayer deposition. (b) Trilayer lift-off. (c) Counter-electrode definition by RIE. (d) SiO$_2$ dielectric deposition and lift-off. (e) Contact hole etch and Al wet etch. (f) Resistor deposition and lift-off. (g) wiring layer deposition and lift-off
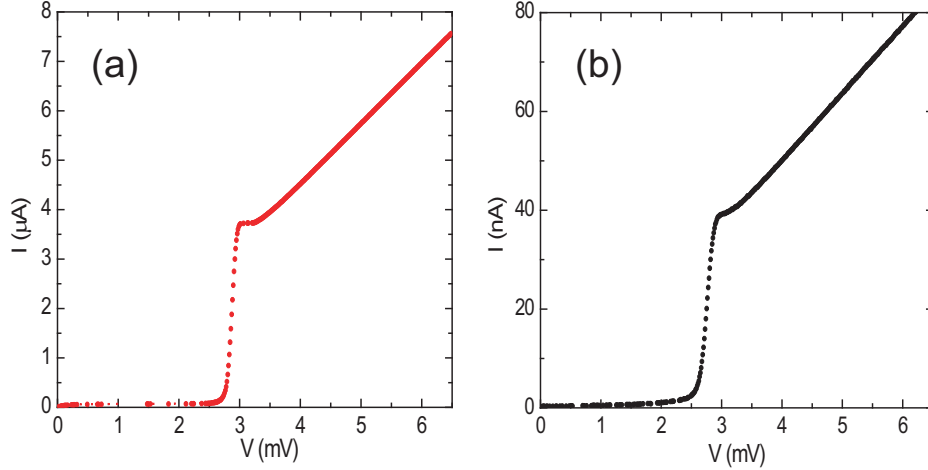
Figure 2.2: Current-voltage characteristic curves at 4.2 K of a (a) 1.4 μm x 1.4 μm junction, $R_N = 800\ \Omega$, $V_g = 2.85$ mV and (b) 0.14 μm x 0.14 μm junction, $R_N = 74$ kΩ , $V_g = 2.75$ mV.

2.2.1 Conductance Scaling

Conductance scaling is obtained by extracting the normal resistance, R_N, from the measured current-voltage (IV) curve of each junction on the test chip. Fig. 2.2 shows representative IV measurements for a 1.4 μm x 1.4 μm and 0.14 μm x 0.14 μm junctions at 4.2 K. The $V_m = I_C R_{qp}(2\text{mV})$ did not change with junction size down to deep-submicron dimensions and was $\sim$50 mV at 4.2 K. Fig. 2.3a shows the scaling of the normal conductance ($G_N = R_N^{-1}$) plotted as $G_N^{1/2}$ with junction design size, L, for two different wafers. The slope of the fit gives the inverse of the scaling factor of the normal resistance, $r_N = R_N \cdot A$. The intercept gives a value $2L_0$, where L_0 is the 'undercut' per side. The value $L_0 = 80$ nm obtained from the conductance scaling data for the two chips shown is in agreement with the physical undercut measured from the SEM image.

2.2.2 Quasiparticle Step (I_{step}) Scaling

The typical value of critical current density (J_c) used for the rf-SQUID qubit is in the range of $\sim$50 A/cm^2 to $\sim$100 A/cm^2 (or 0.5 to 1 μA/μm^2). To characterize the critical current density of the fabricated junctions having low J_c, the quasiparticle step height at the gap voltage, V_g, is measured and calibrated against data of the switching current distribution from junctions larger than 2 μm in size at 4.2 K and 1.3 K. This will give a conversion
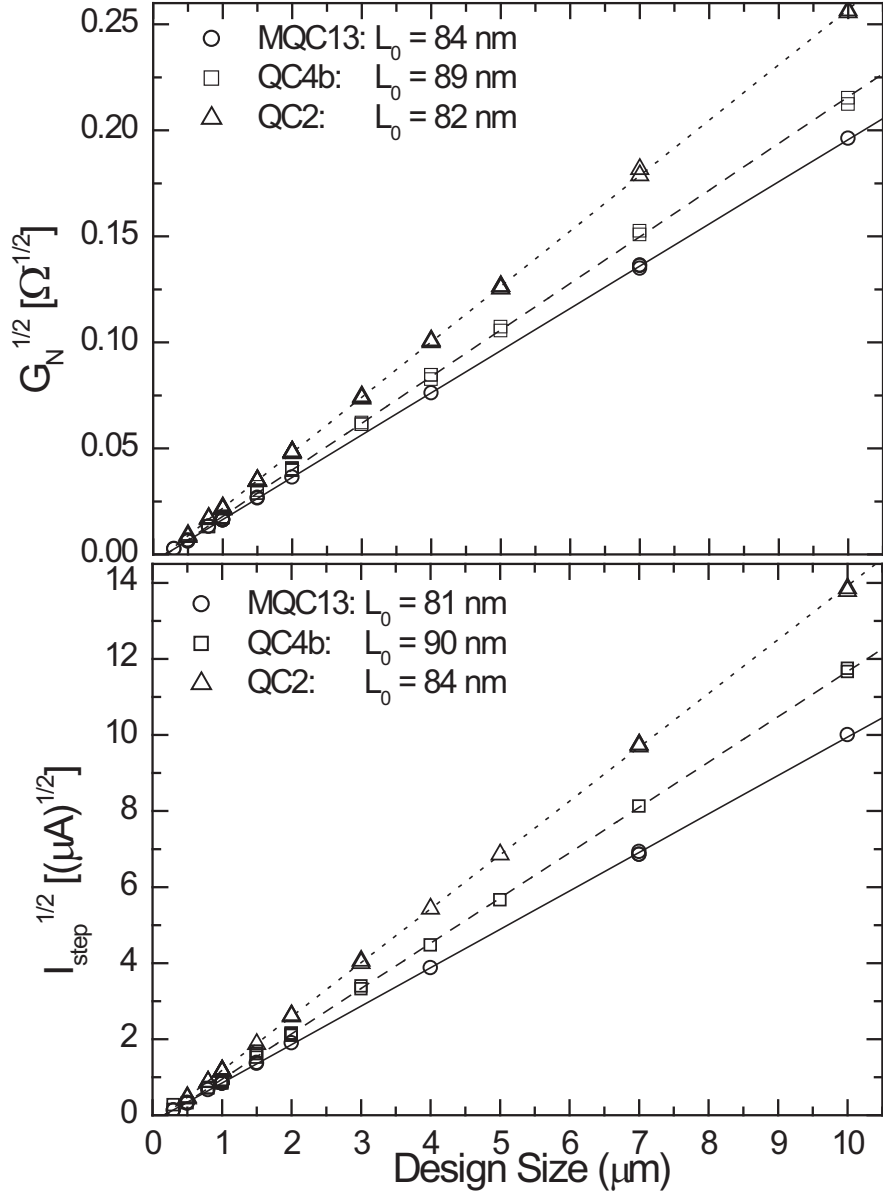
Figure 2.3: (a) Scaling of normal state conductance with design size. Data from three different wafers with current densities 55 A/cm^2 (circles), 80 A/cm^2 (squares), and 105 A/cm^2 (triangles). Lines are linear fits to the data. Assuming the junctions are square, the intercept $2L_0$ gives the etched 'undercut'. (b) Scaling of the quasiparticle current step I_{step} with design size for the junctions in (a). Linear fits give similar values for $2L_0$.

24
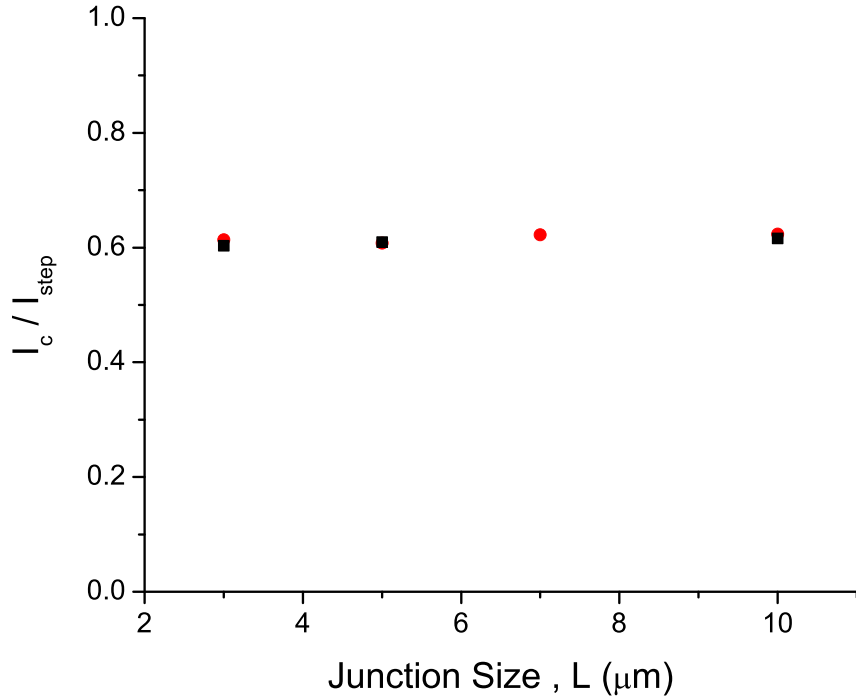
Figure 2.4: χ ratios from switching current distribution measurements of junctions from a single wafer (QC4). Data are shown for measurements at 4.2 K (squares) and 1.3 K (circles), and gives an average value of $\langle \chi \rangle = 0.61$.

factor between current density and the size scaling of the quasiparticle current step and speed up the characterization process of the junction devices. The value of the critical current is obtained from a fit to thermal activation theory [50, 51, 52]. These measurements were performed on junctions of size (L) from 3 μm to 10 μm. Junctions with size 2 μm and smaller must be cooled below 1 K with appropriate microwave filtering to avoid effects of phase diffusion [53] or damping from the leads [54].

The extracted critical current from the switching current data allow for an empirical relation, $I_c = \chi I_{step}$, to be defined, where I_{step} is the quasiparticle current step at $2\Delta/e$ and χ is constant for a given wafer, as shown in Fig. 2.4. I_{step} then may be used for additional statistics to characterize the Josephson junctions, as shown in Fig. 2.3b in which the scaling of I_{step} with junction size is given for the same devices as those in Fig. 2.3a. The value of L_0 obtained from a linear fit of the data in Fig. 2.3b agrees with the result from the

conductance scaling. The similar results lend support toward the assumption that the junctions are square and the effective size is given by $L_{eff} = L - 2L_0$.

Josephson junctions measured from various different wafers gave a 95% yield having good electrical characteristics and a $V_m > 50$ mV. The yield is close to 100% when devices with visually obvious process problems were discounted. The variations in L_0 from wafer-to-wafer is typically between 65-90 nm and is sensitive to overetch process [35].

Chapter 3

Subgap Quasiparticle Transport

It was discussed, in chapter 1, that an intrinsic source damping of the quantum mechanical coherent oscillations of flux in an rf-SQUID qubit is provided by quasiparticle leakage at the oscillation frequency, δ, which we characterized as a resistance, $R(\delta)$. The decay rate was found to be inversely related to $R(\delta)$. Therefore measurement of the quasiparticle current in the subgap regime of the Josephson junction, which we demonstrate in this chapter, is necessary in order to understand the limiting decoherence properties of the rf-SQUID qubit utilizing those junction devices.

3.1 Experimental Design and Setup

Subgap quasiparticle current measurements were performed on unshunted Josephson junctions having sizes of 1.3, 1.8, 4.8, and 9.8 μm. The unshunted junction devices are fabricated using the process discussed in chapter 2. The junctions used in the following measurements were located on test chips used for uniformity characterization of the rf-SQUID qubit critical current density, junction size and normal conductance. Josephson junction samples whose subgap quasiparticle current were measured had a critical current density of 55 A^2/cm or 100 A/cm^2.

The subgap current measurement is a 4-point measurement of an unshunted Josephson junction with its critical current suppressed by an external magnetic field. Room temperature EMI filtering, low-pass cold-filtering, and high-impedance, low-current noise instrumentation amplifiers (utilizing Burr-Brown OPA111 chips) are required for the sensitive measurement of very low currents in high resistance devices. A battery powered voltage reference signal generator for voltage sweeping was used with a high resistance bias box having resistors from 100 kΩ to 10 MΩ for current sensing and limiting of the biased

junctions. The low-pass RC filters having a cut off of 80 kHz ($R = 2$ kΩ, C = 1 nF) are thermally anchored at 4.2 K.

The output from the current and voltage sensing amplifiers connected to the circuit as shown in Fig. 3.1 are measured by HP 34401A multimeters and data is acquired via a personal computer. Any offsets in the voltage and current measurement were accounted for by the symmetry of the data.

A superconducting solenoid magnet, which can produce fields on the order of 10^4 Gauss or greater, was used to suppress the observed switching current to the order of 10^{-5} I_c ($B = 0$) or smaller. Typically, at temperatures of 1.3 K and 4.2 K, the field was changed until the observed switching current and hysteresis seen in the current-voltage curves was not apparently visible on the scale of the subgap current level measured. For temperatures lower than 1.3 K the supercurrent was suppressed to a minimum. This limitation in suppressing the critical current at lower temperatures was possibly due in part to the insufficient current resolution of the magnet power source, which was a 1.5 A, 18 V (27 W) Harrison model 855B power supply modified for manual analog control of the magnet current bias, and partly due to irregularities in the shape of the Josephson junction [55].

The sample chip is mounted on a 68-pin gold lead chip carrier with aluminum base. Electrical contact to the junctions are provided by Al wire bonds. The sample is situated in the cryostat such that the magnetic field threads through the plane of the junction tunnel barrier, as seen in the inset of Fig. 3.1. The sample can be placed in a cryostat probe designed for dipping in a LHe bath, which can be pumped to cool the dipping probe down to 1.3 K, or in a ^{3}He cryostat that can cool the sample down to 0.35 K.

For the measurements in the range of $T < 1.3$ K, the carrier with chip is inserted into a sample cell that is mounted onto a ^{3}He cryostat. The cryostat is constructed in a typical design where at 4.2 K ^{3}He is stored in a charcoal sorb cooled by a bath of liquid He (LHe). A pot that is continuously filled with LHe from the bath through a long, thin stainless steel impedance tube can be pumped to cool the LHe pot to 1.3 K. Heating the charcoal sorb to roughly 20 K releases ^{3}He gas where it can condense at the ^{4}He pot and collects in another pot below (^{3}He pot). After the ^{3}He is condensed, the charcoal sorb is cooled back down to 4.2 K and begins to pump on the ^{3}He bath to a temperature that then reaches $\sim$0.35 K in our cryostat. A platform connected to the ^{3}He pot allows for samples to be mounted and cooled. Temperature variation control is performed via a wire-wound resistor on the platform while the temperature is monitored by a RuO$_x$ (from Scientific Instruments) thermometer mounted to the sample platform.

Modulation of the critical current, I_c, in an applied field was observed in all
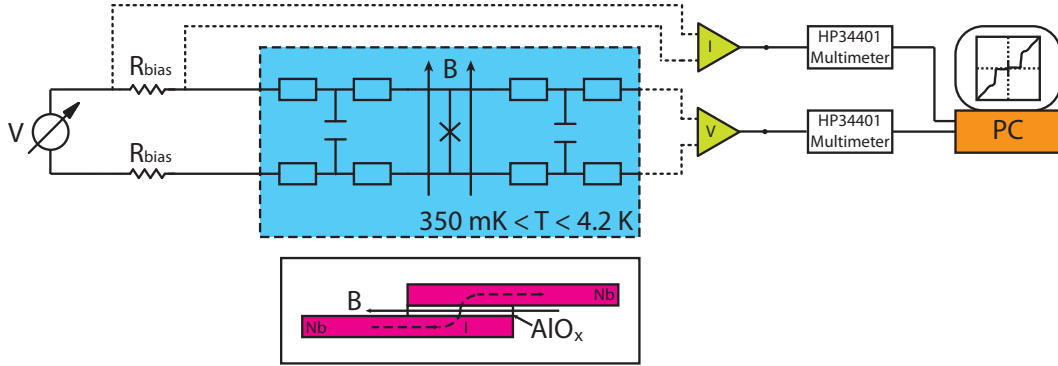
Figure 3.1: Diagram of the electrical setup for subgap I-V measurements of unshunted Josephson junctions. The magnetic field lines represent the junction device being situated in a solenoid for suppression of the critical current. The inset shows the direction of the field through the tunnel barrier.

junctions studied. The modulation of the critical current followed the expected Fraunhofer-like diffraction pattern, which takes the form of Eqn. 1.13. Fig. 3.2 shows the critical current modulation of a 1.5, 2, 4, and 10 μm junctions at 4.2 K as a function of applied flux, $\Phi = B \cdot A$. There is slight deviation between the position of the measured minima of I_c in data at larger field and the expected minima values of the "ideal" junction from Eqn. 1.13. Again, as mentioned above, irregularities in the shape of the junction [55] may lead to this disagreement between experiment and theory.

3.2 Subgap Current Characteristics

Junction samples in which the low-voltage subgap quasiparticle current was measured included a 1.7 μm^2, 3.2 μm^2, 23 μm^2, and 96 μm^2 sizes. At 4.2 K, the subgap current data was acquired for bias voltages from 0 to 2.5 mV at 4.2 K, and at 1.3 K from 0 to $\sim$0.8 mV as observed in Fig. 3.3. For the corresponding temperatures, comparison with the BCS calculation (Eqn. 1.11) of the quasiparticle current is shown as the solid line in Fig. 3.3.

Typically, comparison of the measured I-Vs with the BCS calculation showed good qualitative agreement at low voltages and was about a factor of 1.5 to 2 times larger than BCS for the temperature range between 1.3 K
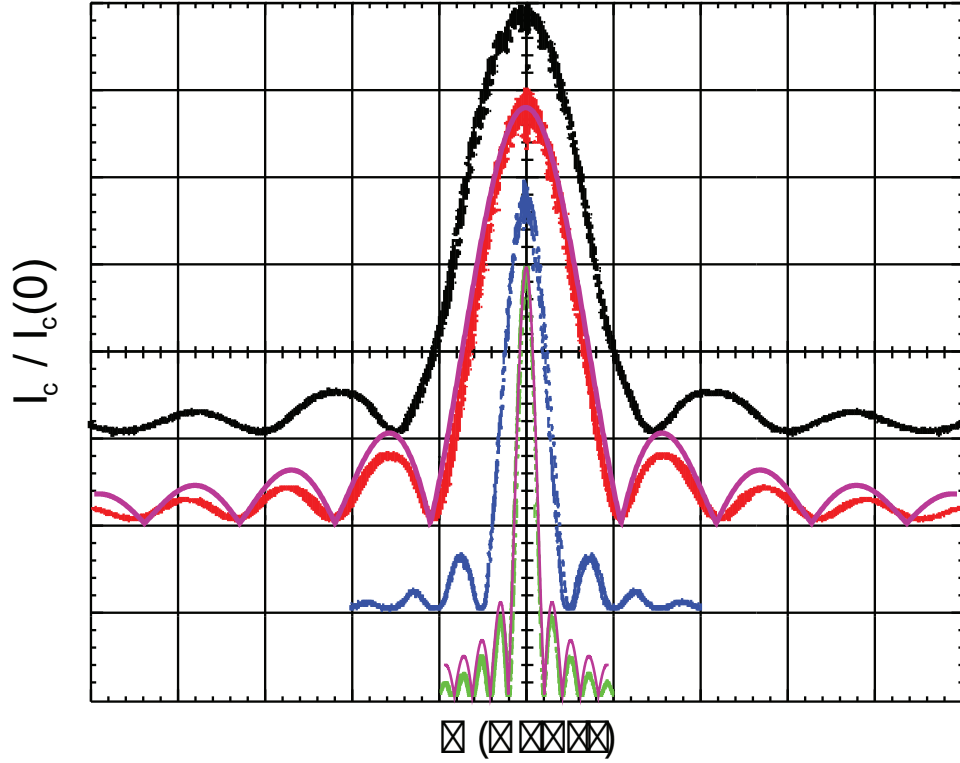
Figure 3.2: Modulation of the switching current (from top to bottom) of a 1.3, 1.8, 3.8, and 9.8 μm size junctions at 4.2 K. The curves are normalized to their maximum critical current at zero field ($B = 0$) and offset to better view them on the graph. The solid purple curves are Eqn. 1.13 calculated for the 1.8 and 9.8 μm size junctions, respectively. The first minima of the modulation curves are 100, 71, 34, and 13 Gauss for respectively the 1.3, 1.8, 3.8, and 9.8 μm size junctions.
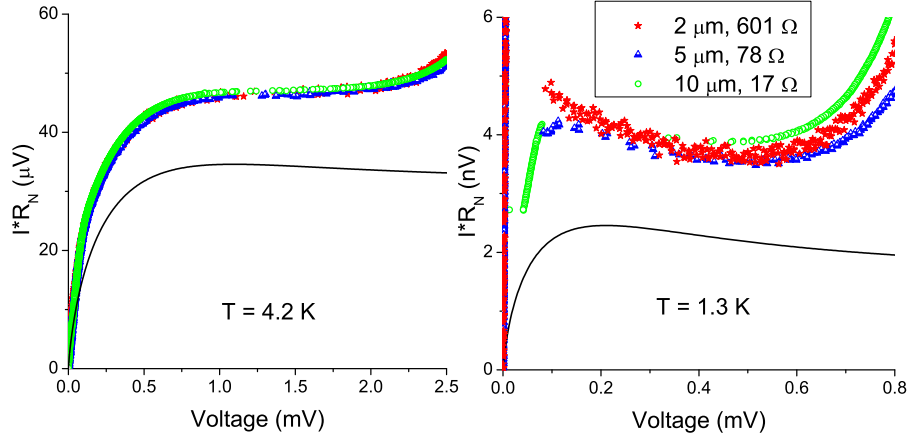
Figure 3.3: Residual subgap currents at a) 4.2 K and b) 1.3 K for three junctions of size 1.8 μm (stars), 4.8 μm (triangles) and 9.8 μm (circles) normalized to G_N. The solid lines are BCS calculations using Eqn. 1.11.

and 4.2 K. Subgap current-voltage data acquired for 1.7 μm^2 and 3.2 μm^2 junctions at 360 mK and 400 mK, respectively, is shown in Fig. 3.4. A temperature series of junction samples from 360 mK to 4.2 K of the resistance at 0.5 mV ($R_{sub}(0.5$ mV$) = 0.5$ mV$/I_{sub}(0.5mV)$) normalized by R_N is shown in Fig. 3.6. We recall from chapter 1 that R_{sub}/R_N is a convenient parameter that tends to follow the expected Q for the rf-SQUID qubit system and allows for comparison of junctions of various size. The results show in Figs. 3.4 and 3.6 that around 400 mK the ratio of subgap resistance to normal resistance of the junction is larger than 10^6. When compared with the BCS calculation at 0.5 mV, the data reveals a saturation in the leakage current for temperatures below 1 K.

The increase in the quasiparticle subgap current approaching $V_g/2$ seen in Fig. 3.4 and the temperature series measurement of the IV curves in Fig. 3.5 is suggestive of combined single and double quasiparticle tunneling effects [56] or of impurities or defects in the barrier. Therefore, saturation in the leakage current at 0.5 mV $< V_g/2$, as seen in Fig. 3.6, may be due to these excess tunneling processes. Alternatively, this saturation in the leakage current at temperatures below 1 K has also been reported elsewhere [21, 22] and is possibly due to damping effects from the bias leads [54].

The above results shown in Fig. 3.6 represent the quasiparticle resistance at a voltage corresponding to a frequency 200 times larger than the energy level splitting frequency mentioned in chapter 1 ($\delta \sim 10^9$ Hz), which is where
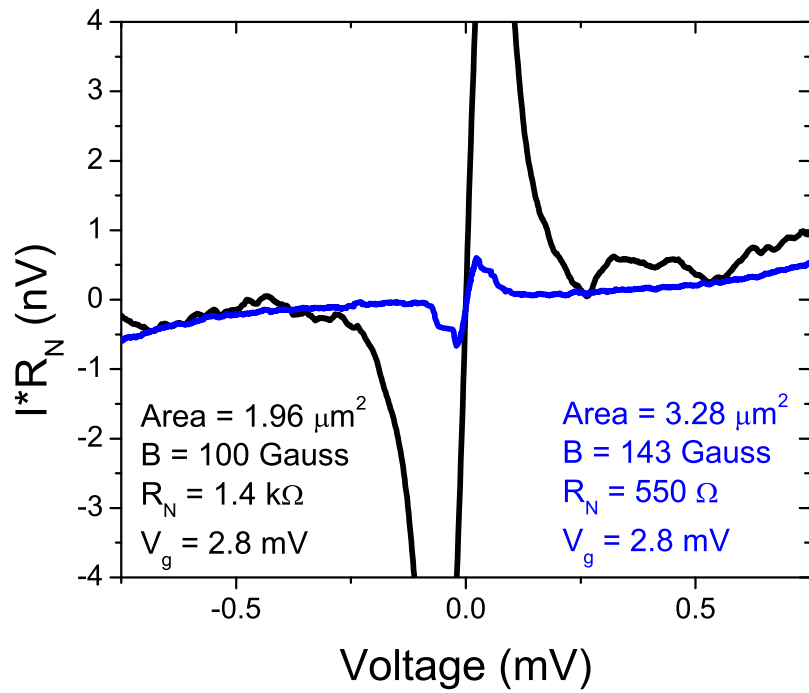
Figure 3.4: Residual subgap currents at 0.36 K and 0.4 K for 1.7 μm^2 (black) and 3.3 μm^2 (blue) junctions respectively.
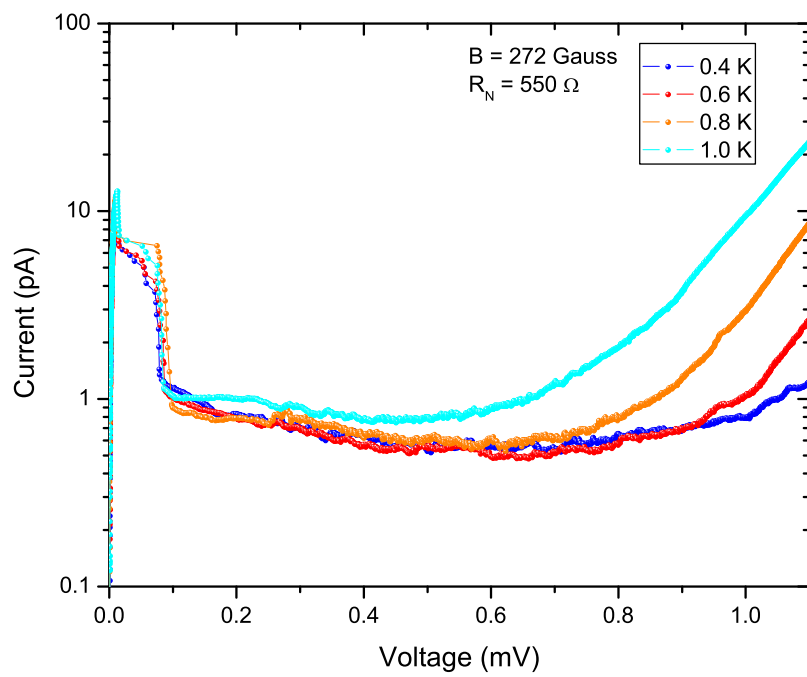
Figure 3.5: Temperature series of the subgap current for a 1.7 μm^2 junction from 0.4 K to 1 K in a magnetic field of $B = 272$ Gauss.
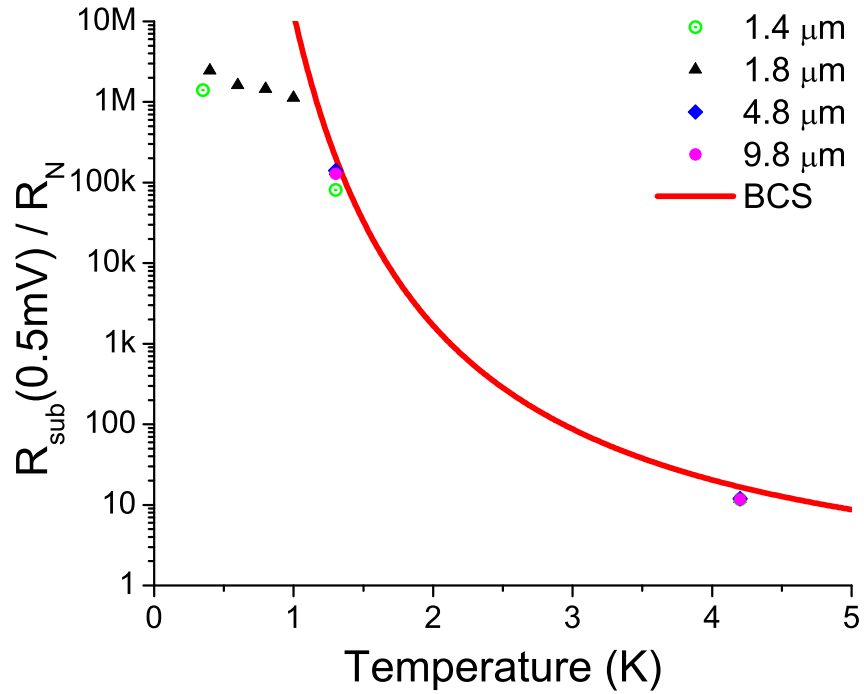
Figure 3.6: Normalized resistance at 0.5 mV as a function of temperature in a 3.3 μm^2, 23 μm^2 and 96 μm^2 junctions with critical current suppressed by magnetic field. The solid red line is the expected normalized BCS quasiparticle resistance.

the Ohmic damping will be important in the rf-SQUID qubit. The level of the BCS quasiparticle current at a voltage corresponding to δ is expected to be much smaller than the current level at 0.5 mV for 400 mK. We take the optimistic approach and make the argument that the quasiparticle resistance is relatively constant down to the μV bias range based on the IV characteristics presented in Fig. 3.4. The results shown in Fig. 3.6 set an upper bound on the effects of Ohmic damping in the rf-SQUID qubit. Thus, we expect that the coherence time of the qubit should not be limited by Ohmic damping.

Chapter 4

Low Frequency Critical Current Fluctuations

The intrinsic low frequency $1/f$ critical current fluctuation noise in Josephson junctions is a source of decoherence in flux qubits [4, 57] as discussed earlier in chapter 1. The origin of this noise is not completely understood, but it is generally believed to be caused by charge traps in the oxide barrier of Josephson junctions [41, 42, 43]. Measurements of $1/f$ critical current fluctuations in Josephson junctions at zero voltage using a dispersive method have demonstrated that critical current fluctuations measured at non-zero voltage are equal [26], which provides a quantitative basis for measurements of critical current fluctuations in junctions biased in the dissipative state and the inferred decoherence in flux based qubits.

Many measurements of critical current fluctuations in Josephson junction devices have been performed over the last few decades [27, 28, 38, 58, 59, 60], but the temperature dependence of the critical current fluctuations is less understood. This issue has become particularly important in the context of understanding decoherence in superconducting qubits.

Critical current fluctuations measurements in SQUID magnetometers [27] showed that the temperature dependence of the spectral density of critical current fluctuations at 1 Hz, $S_{Ic}(1Hz)$, follows T^2 down to mK temperatures. In another experiment [28], it was found that the spectral density at 1 Hz of resistance fluctuations measured in Al/AlO$_\text{x}$/Al junctions via suppression of the supercurrent in the junction was *linearly* dependent upon temperature. Table 4.1 shows other measurements of noise in Josephson junctions and the associated measured temperature scaling. With no firmly established microscopic model for the temperature dependence of critical current fluctuations [41, 42], it becomes imperative to understand the temperature scaling of S_{Ic} in order to help identify its mechanism.

Table 4.1: Temperature scaling of $1/f$ noise in Josephson junctions from various device technologies.

Device Technology	Noise Measurement	Temperature Scaling
Al/AlO$_x$/Al Ref. [60]	charge	T^2
Nb/NbO$_x$/PbIn Ref. [27]	critical current	T^2
Al/AlO$_x$/Al Ref. [61]	charge	T^2
Al/AlO$_x$/Al Ref. [28]	resistance	T

4.1 Experimental Design

Care must be taken in the design of the Josephson junction in order to observe critical current fluctuations. In part of the following experiments, noise in unshunted junctions is measured above the gap voltage at 4.2 K. In Nb/AlO$_x$/Nb junctions, the measurements of S_{Ic} from conductance fluctuations above the gap voltage does not lend to itself the ability to accurately determine S_{Ic} for temperatures near 1 K and lower due to electron bath heating via the hot electron effect at finite voltage bias.

A resistively shunted junction (RSJ) device allows one to bias the junction near the critical current to reduce heating in the junction. Given this, however, there is still considerations involved with optimizing the design of the RSJ device in order to maximize the level of critical current fluctuations relative to the Johnson noise of the shunt resistor and minimize heating effects in the shunt resistor for the measurement of the noise. With this in mind, hot electron effects in an external shunt resistor of the Josephson junction will be discussed after first describing the experimental setup and measurement scheme. This will be followed by a discussion of the design parameter and bias current dependence of the current fluctuations, S_I, in an RSJ device. While not being a primary factor in the experimental design of the RSJ devices, the design parameter and bias current dependence of current fluctuations in unshunted Josephson junctions will be discussed to facilitate the analysis and discussion of the data from the measurements in §4.2.2 and §4.2.3.
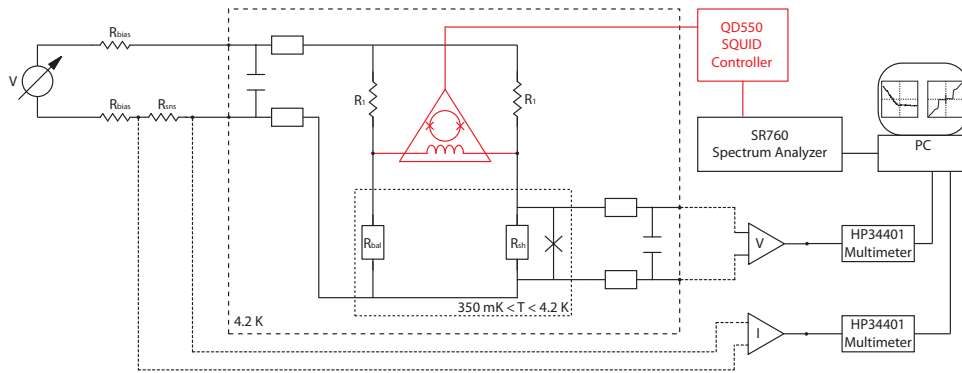
Figure 4.1: Diagram of the electrical setup for current noise measurement and data acquisition. The configuration shown is for measurement of a resistively shunted Josephson device.

4.1.1 Electronics Setup and Measurement

The measurement of current noise is performed with a Wheatstone bridge circuit, and uses a commercial dc-SQUID preamplifier [62] as a null current detector to measure the total current noise of the circuit, as illustrated in Fig. 4.1. Depending on the device to be studied, such as an RSJ, unshunted JJ, or thin film test resistors, the bridge circuit is modified according to the characteristics of the device.

For the resistively shunted junction, the shunt resistor, R_{sh}, and an identical thin film balancing resistor, R_{bal}, are both fabricated on the same sample chip to comprise one half of the bridge circuit (the "lower" bridge), as seen in the optical photograph in Fig. 4.2. In this configuration, the balancing resistor, R_{bal} was selected to match the external shunt resistance, R_{sh}. The remaining half of the bridge circuit (the "upper" bridge) is balanced by identical resistors, R_1, that are much larger than R_{bal}, or R_{sh}. For measurements of unshunted junctions, the balancing resistor, R_{bal}, is a metal thin film 1% precision resistor anchored at the same temperature as the sample chip and chosen to match the junction normal resistance, R_N. All other components are the same for this setup as for the shunted junction setup.

For current noise measurements solely of the shunt resistors, R_{sh}, for the RSJ devices, copies of the thin film test resistor identical to R_{bal} shown in Fig. 4.2 were fabricated on a separate chip from the RSJ bridge devices. They were fabricated to make a circuit to complete the "lower" half of the Wheatstone bridge circuit similar to the "lower" bridge RSJ circuit previously mentioned.

Current noise measurements were performed with the bridge circuit set up in a ^{3}He cryostat in order to measure below 1.3 K. Details on the cryogenic
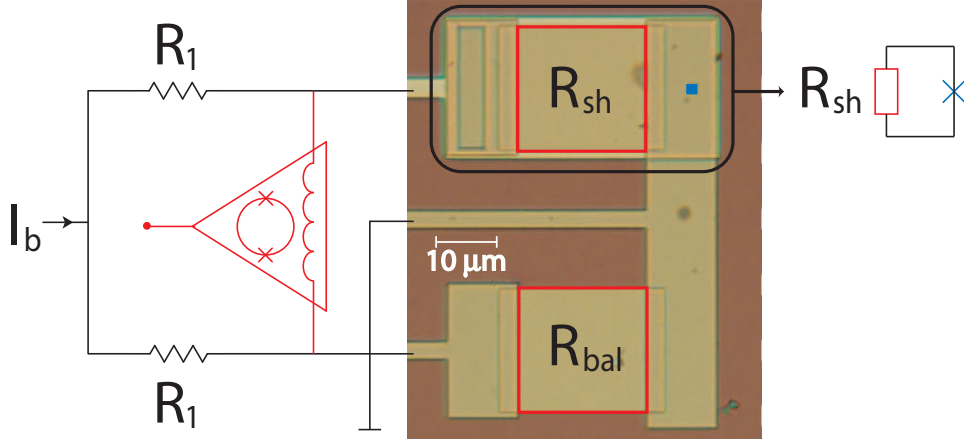
Figure 4.2: Diagram showing a close-up of the bridge circuit for current noise measurements including an optical photo of the 2 μm on-chip RSJ device and balancing resistor.

components and operation of the ^{3}He cryostat are given in §3.1. Some current noise measurements were also performed using a dipping probe. The sample is mounted on one end on the inside of the probe and is enclosed by a vacuum tight can. By evacuating the probe and adding He exchange gas, a thermal link is provided between the sample and the liquid He cooling bath, which can be pumped in order to cool the dipping probe and sample from 4.2 K to 1.3 K.

As shown in Fig. 4.1, room temperature electronics include a battery powered voltage source, symmetric current bias resistors, a current monitor resistor, EMI filters, cold low-pass filters, and instrument amplifiers. The electrical leads of the voltage source are connected to the current monitor resistor and symmetric bias resistors. The symmetric bias resistors are metal thin film resistors which can be selected to have values from 2 kΩ to 20 MΩ in order-of-magnitude increments. The electrical leads then pass through EMI filters to cut off high frequency signals. The leads from the room temperature electronics then pass into the cryostat through a vacuum-tight electrical feedthrough. From the feedthrough, the leads connect to low-pass RC filters thermally anchored at 4.2 K. In the ^{3}He cryostat, the electrical leads making connection from room temperature to 4.2 K are composed of thermally resistive and electrically insulated phosphor bronze wiring, which has a resistance per unit length of roughly 10 Ω/ft. CuNi wire is used to make electrical connections between 4.2 K and the ^{3}He stage. The low-pass cut-off of the cold filters is 8 kHz ($R = 200\Omega$, $C = 0.1$ μF). Leads to monitor the voltage across the junction device are also connected. These leads are cold
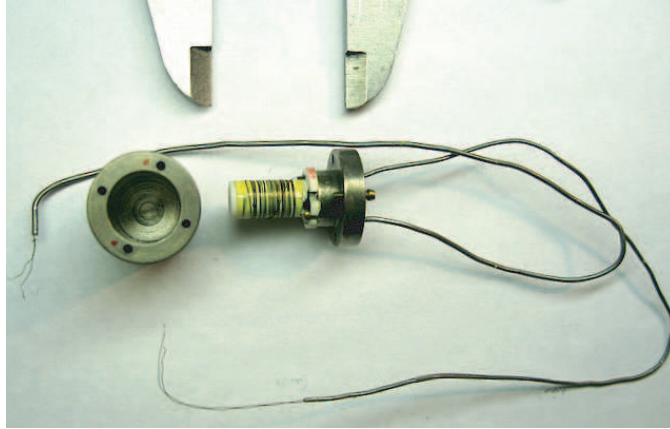
Figure 4.3: Image of the superconducting transformer with concentric solenoids, its NbTi shielding capsule, and Pd tube shielded leads for the primary and secondary coils. The scale of the calipers is 1 in.

filtered and EMI filtered as described above. The voltage and current sensing leads are connected to instrument amplifiers and their voltage output is read by HP34401 multimeters. The data from the multimeters is then acquired by a personal computer to be analyzed later.

Electrical connections to the SQUID detector or superconducting transformer are accomplished through pressure contacts. For connection to the SQUID detector, the wire is stripped then is connected by screwing together a brass washer onto the wire and a niobium pad. The electrical contact to the niobium is made by pressure from the washer on the wire, which typically provides adequate pressure for good electrical contact even after several thermal cycles.

Connections for the superconducting transformer are accomplished in the same manner. Shielding of the superconducting wire leading to the SQUID from the transformer is important to eliminate flux noise that can be generated by the loop of superconducting wire. Shielding of the twisted pair wire is provided by lead tubing, which becomes superconducting at roughly 7 K. For the transformer, the pressure joint connector is machined NbTi that houses the pressure joints. A NbTi clamp allows for the shielded twisted pair wire to be secured to the housing. A NbTi cover provides shielding of the joints in the housing. Figure 4.3 shows the superconducting transformer and shielding devices for electrical connection between the DC SQUID magnetometer and bridge circuit.

The SQUID detector is connected to a Quantum Design Model 550 controller [62], which biases and modulates the dc-SQUID in a flux-locked

39
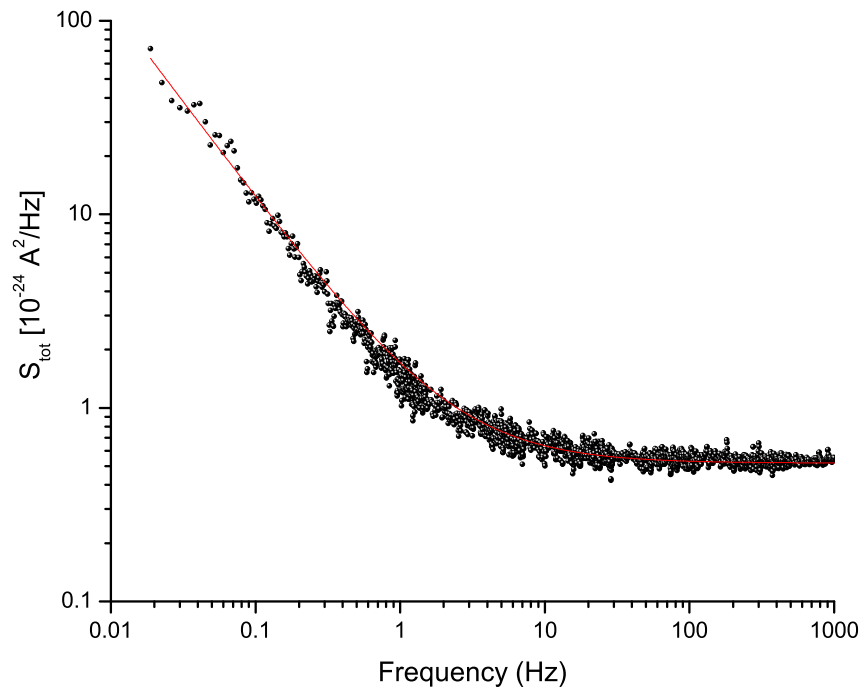
Figure 4.4: Total current noise spectra of the Quantum Design model QD50 DC SQUID sensor output at 4.2 K. The input coil to the sensor was shorted using a ~1 cm Nb or NbTi wire.

feedback loop in order to have a voltage output from the controller that is proportional to the current through the input coil of the SQUID detector. The proportionality of the output voltage to input coil current is given by the ratio of the input coil coupling $(\Delta I/\Phi_o)$ to the voltage-to-flux transfer function ratio $(\Delta V/\Phi_o)$ of the dc-SQUID. For the SQUID detector used in these experiments and for its maximum sensitivity range, the proportionality constant takes the value of 0.27 pA/μV ($\Delta I/\Phi_o = 0.194$ μA/Φ_o, $\Delta V/\Phi_o$).

The commercial dc-SQUID preamplifier [62] has an equivalent input current noise of $(0.53 \pm 0.03) \cdot 10^{-24}$ A^2/Hz at 1 kHz and a $1/f$ component of $(1.2 \pm 0.10) \cdot 10^{-24}$ A^2/Hz at 1 Hz. Spectral measurement of the DC SQUID output signal having its input coil shorted by Nb wire at 4.2 K is shown in Fig. 4.4. We can modify the measurement setup in Fig. 4.1 by inserting into the bridge circuit the primary coil of a superconducting transformer, where the secondary coil is then connected to the SQUID input coil. This effectively reduces the background noise of our SQUID detector to $0.004 \cdot 10^{-24}$ A^2/Hz, with a 1 Hz value of about $0.012 \cdot 10^{-24}$ A^2/Hz.

The output from the SQUID controller is then connected to a Stanford Research Systems model SRS760 spectrum analyzer, which has a 100 kHz bandwidth and a minimum frequency resolution of 477 μHz. The spectrum analyzer computes the FFT of the digitized input signal and outputs the power spectral density. The spectral data for a given measurement was typically acquired in the frequency spans of 0-6.1 Hz, 5-29.4 Hz, 10-107.5 Hz, 100-490 Hz, and 400-1960 Hz. The frequency resolution of each span is equal to the span divided by 400, which respectively gives 15 mHz, 61 mHz, 244 mHz, 975 mHz, and 3.9 Hz. For each respective frequency span the spectral density was typically acquired 300, 500, 750, 1000, and 1500 times and respectively averaged. To increase the data acquisition time for the full set of frequency spans, the overlap of data between the successive spectral acquisitions was set at 90%. The resultant averaged spectra from each span is then acquired by a personal computer from the spectrum analyzer, combined into a spectra spanning typically 0.1 Hz to 1 kHz, which comprises the spectral measurement, and stored for later analyzing.

4.1.2   Hot Electron Effects

Externally shunting the Josephson junction allows for the reduction of the bias current required to measure S_{Ic}, thereby reducing the dissipated power in the junction compared to that when biasing above the gap voltage, V_g, in unshunted JJs. Providing that the shunt resistor is in good thermal equilibrium with the bath temperature and its volume and electron-phonon coupling allow for adequate energy transfer between the electron and phonon bath of

the resistor [63], then the thermal equilibrium electron bath temperature of the resistor will closely follow the power dissipated in the shunt resistor via a power law heating model given by

$$T_e\left(P\right) = \left[\frac{P}{\Sigma\Theta} + T_o^5\right]^{\frac{1}{5}}, \tag{4.1}$$

where the phonon bath temperature is T_o, which we take to be the same as the bath temperature, P is the power dissipated in the shunt resistor (and we take to be Ohmic), Σ is a parameter related to the electron-phonon scattering rate and dependent upon the material[63], and $\Theta = LWt$ is the solid volume of the shunt resistor with L, W and t its length, width and thickness. The Johnson noise of a resistor gives a measure of its electronic thermal equilibrium temperature, as seen in Eqn. 1.16. We rewrite the expression in its spectral density form as

$$S_n = \frac{4k_B T_e}{R}, \tag{4.2}$$

where $S_n = I_n^2$, and assign T_e for T. By measuring the current spectral density of a resistor as a function of applied bias, the electron bath temperature can be calculated and compared with the heating model of Eqn. 4.1 to determine if any hot electron heating effects occur, especially for bath temperatures, T_o, below 1.3 K.

In our initial design, for junction device samples having 55 A/cm^2 critical current density, we modified the Josephson junctions that were originally designed for uniformity characterization of the rf-SQUID qubit critical current density, junction size and normal conductance. In modifying these devices, we were restrained in fabricating the external AuPd shunt resistors to have small volumes and achieve a $\beta_c < 0.5$. Therefore, the bias range to measure spectral current noise in the resistor was determined such that the electron bath temperature of the resistor would not deviate much from the bath temperature, T_o. Heating of the electron bath of roughly 3% greater than the bath temperature while at 1.3 K occurred at approximately 425 μV for resistors designed to shunt a 2 μm sized junction. This "critical" bias point decreased by two orders of magnitude to about 3.5 μV upon cooling to 345 mK, and is shown in Fig. 4.5, making hot-electron heating in the junction an issue at all practical bias points at this lowest temperature.

In a subsequent design to study critical current fluctuations in RSJ devices having ∼570 A/cm^2 critical current density, the AuPd resistors were fabricated with an appropriate volume according to Eqn. 4.1 such that biased near the critical current and at 350 mK there should be minimal increase in the electron bath temperature above the bath temperature. The measured electron bath
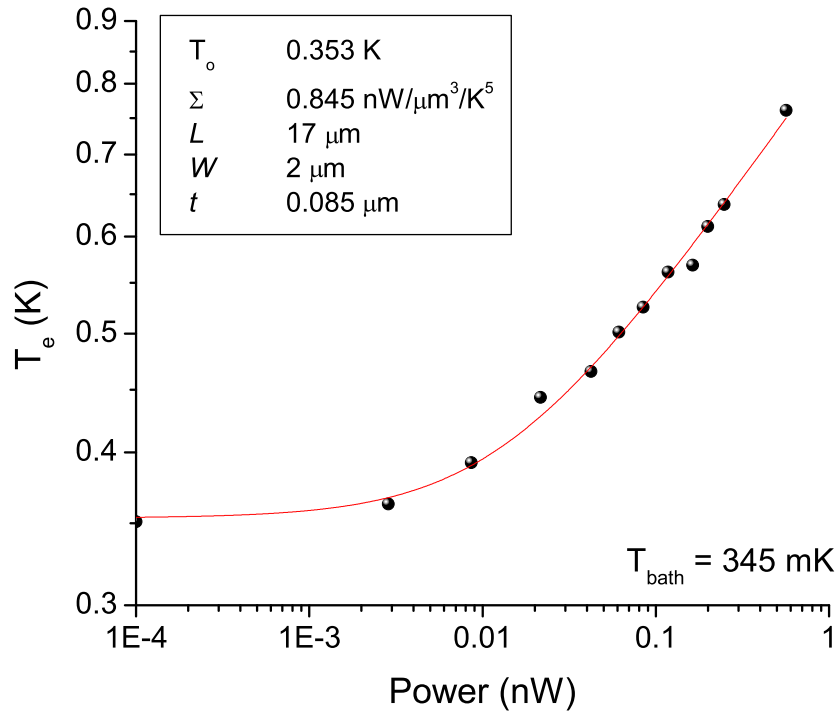
Figure 4.5: Electron bath temperature for a AuPd resistor ($R = 9.6\ \Omega$) versus dissipated power at a bath temperature of 345 mK. The parameters, Σ and T_o were free variables in the fit of the data shown above, where all other parameters were fixed.
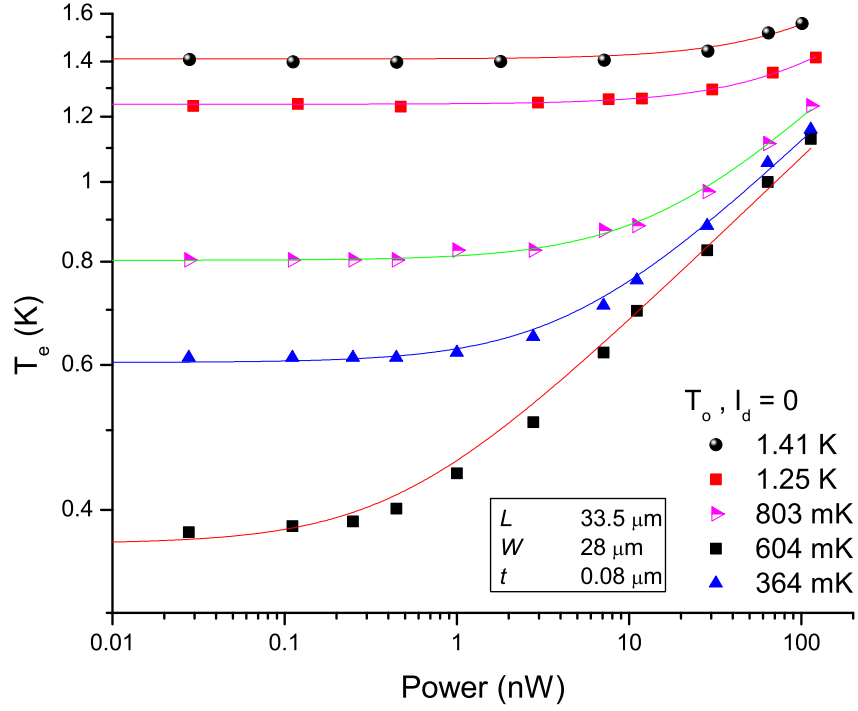
Figure 4.6: The electron bath temperature versus dissipated power in a AuPd resistor ($R = 4.2\ \Omega$) at a bath temperatures of 373 mK, 596 mK, 796 mK and 1.25 K. To the left of the solid vertical line indicates the region of dissipated power when measuring current noise in the RSJ devices. The extracted value of $\Sigma = 0.95\ \mathrm{nW}/\mu\mathrm{m}^3/\mathrm{K}^5$ at $T = 373$ mK is similar to the value extracted from the data in Fig. 4.5.

44
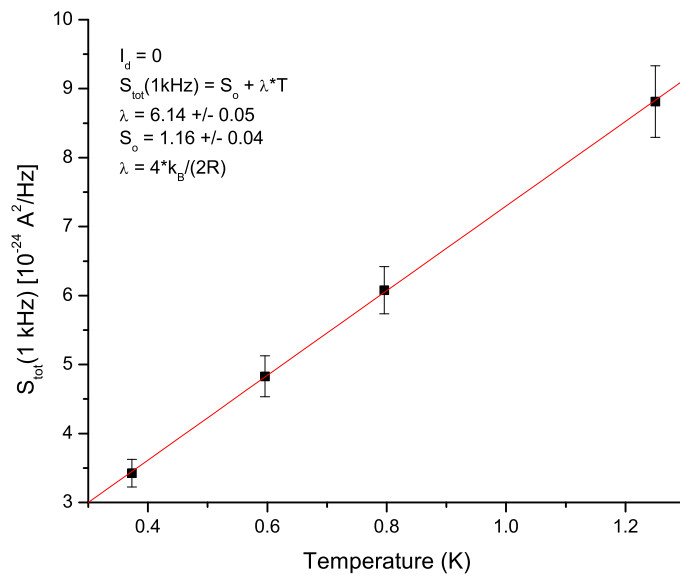
Figure 4.7: Zero bias spectral current noise at 1 kHz of two 4.5 Ω AuPd resistors in series as a function of temperature. The slope of the curve gives back the resistance of the two AuPd resistors in the bridge circuit. The intercept,S_o, gives the measure of the background circuit noise.

temperature of resistors designed for 2 μm x 2 μm RSJ devices are presented below.

The data of the measured electron bath temperature shown in Fig. 4.6 were fitted with the power law equation (Eqn. 4.1) to extract T_o and Σ. The measured current noise at zero bias shown in Fig. 4.7 indicated that a temperature independent noise was present as was also measured (not shown) in the electron heating curve in Fig. 4.5. The zero bias spectral noise as a function of temperature revealed from a linear fit to the data an offset noise of $S_o = (1.16 \pm 0.04) \cdot 10^{-24}$ A^2/Hz while the slope of the fit gives back the expected resistance of the two AuPd resistors in series, or $R = (9.00 \pm 0.07)$ Ω. Subtraction of this offset noise gives the expected Johnson noise temperature when compared with measurements of the bath temperature using a calibrated RuO thermometer. The principle result of the measurement indicates no heating for up to 1 nW bias for temperatures down to roughly 600 mK. For temperatures below 600 mK, these measurements provide a calibration for the RSJ device temperature for current noise measurements at the lowest temperatures.

4.1.3 Noise Sensitivity Optimization

Optimization of the sensitivity of the noise measurement to critical current fluctuations is essential to the design of the RSJ devices in this experiment. As discussed in the previous section, initial RSJ devices were designed ad hoc using Josephson junctions intended only for characterization of the rf-SQUID qubit current density, and, further, the sensitivity to critical current fluctuations was not fully considered. This resulted in low levels of measured low-frequency $1/f$ signal at 1 Hz to the background white noise making current spectral noise measurement difficult and time consuming.

To investigate improving the measurement sensitivity to critical current fluctuations in an RSJ device its total spectral current noise is analyzed in terms of the current bias and design parameters of the RSJ, such as J_c and β_c. The total noise considered from the resistively shunted Josephson junction, S_{RSJ}, at a particular bias point is the current fluctuations, S_J, due to critical current fluctuations, S_{Ic}, which we assume to have a $1/f$ frequency dependence, and the Johnson noise, S_I (Eqn. 1.18), so that the total current noise is written as

$$S_{RSJ} = S_I + S_J. \tag{4.3}$$

By dividing S_{RSJ} by S_I the above expression can be written in terms of the

ratio of S_J to the Johnson noise, S_I, or

$$\tilde{S}_{RSJ} = 1 + \frac{S_J}{S_I} = 1 + S_{sens}, \tag{4.4}$$

so that S_{sens} is a term that indicates the relative levels of noise in the RSJ device.

The current fluctuations due to the critical current fluctuations are proportional to each other via the model dependent I-V characteristic of the RSJ, and is given by

$$S_J = S_{Ic} \left(\frac{\partial I}{\partial I_c} \right)_V^2, \tag{4.5}$$

where the subscript of the differential denotes differentiation with V held constant. Therefore, the total current noise from the RSJ device can be written as

$$S_{RSJ} = S_I + S_{Ic} \left(\frac{\partial I}{\partial I_c} \right)_V^2, \tag{4.6}$$

The proportionality constant, $\left(\frac{\partial I}{\partial I_c} \right)_V$, can be written in terms of two partial derivatives of the I-V characteristic using the cyclic relation

$$\left(\frac{\partial I}{\partial I_c} \right)_V = - \left(\frac{\partial V}{\partial I_c} \right)_I \left(\frac{\partial V}{\partial I} \right)_{I_c}^{-1}. \tag{4.7}$$

The two partial derivatives in the above equation are now calculated to determine its bias dependence. The ideal I-V relation for the RSJ having no thermal fluctuations (Eqn. 1.7) is used here for completeness of the expressions rather than Eqn. 1.8, which includes thermal fluctuation effects. Later, calculation of the proportionality constant (Eqn. 4.7) including thermal fluctuation effects will be discussed.

Beginning, then, with the I-V expression $V = R \left(I^2 - I_c^2 \right)^{1/2}$, which is only valid for $I > I_c$, the two partial derivatives in Eqn. 4.7 are calculated to be

$$\left(\frac{\partial V}{\partial I} \right)_{I_c} = \frac{RI}{\left(I^2 - I_c^2 \right)^{1/2}} \tag{4.8}$$

and

$$\left(\frac{\partial V}{\partial I_c} \right)_I = - \frac{RI_c}{\left(I^2 - I_c^2 \right)^{1/2}}. \tag{4.9}$$

47
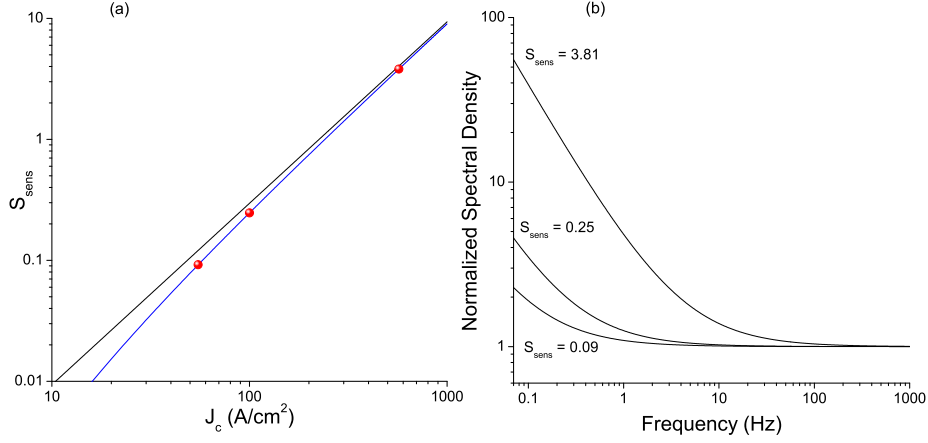
Figure 4.8: (a) Noise sensitivity ratio, S_{sens}, versus designed critical current density at 4.2 K from Eqn. 4.13 (black). The blue curve is the noise sensitivity ratio including thermal fluctuations calculated using Eqn. 1.8. (b) Example normalized spectra density, $\tilde{S}_{RSJ}(f)$, for J_c values of 55, 100, and 570 A/cm², which are respectively the three points along the sensitivity ratio curve in (a).

So that in using Eqn. 4.7 we can write

$$\left(\frac{\partial I}{\partial I_c}\right)_V = \frac{I_c}{I}. \tag{4.10}$$

We see here by substituting Eqn. 4.10 into Eqn. 4.5 that while biased above I_c the current fluctuations due to the critical current fluctuations in the RSJ decreases with increasing bias current, I.

The ratio of current noise due to the critical current fluctuations and the Johnson noise from the RSJ, $S_{sens}(T)$, is now analyzed to find an expression dependent on the RSJ parameters and bias for a given temperature, T. The expression is written

$$S_{sens}(T) = \frac{S_{Ic}(T)\left(\frac{\partial I}{\partial I_c}\right)^2}{S_I(T)} = \frac{S_{IcN}(T)\left(\frac{I_c^2}{A}\right)\left(\frac{\partial I}{\partial I_c}\right)^2}{\frac{4k_BT}{R}\left[1 + \frac{1}{2}\left(\frac{I_c}{I}\right)^2\right]}, \tag{4.11}$$

where S_{Ic} is replaced with the expression for the normalized critical current fluctuations (Eqn. 1.20), R is substituted with the expression for β_c, and I_c is

48
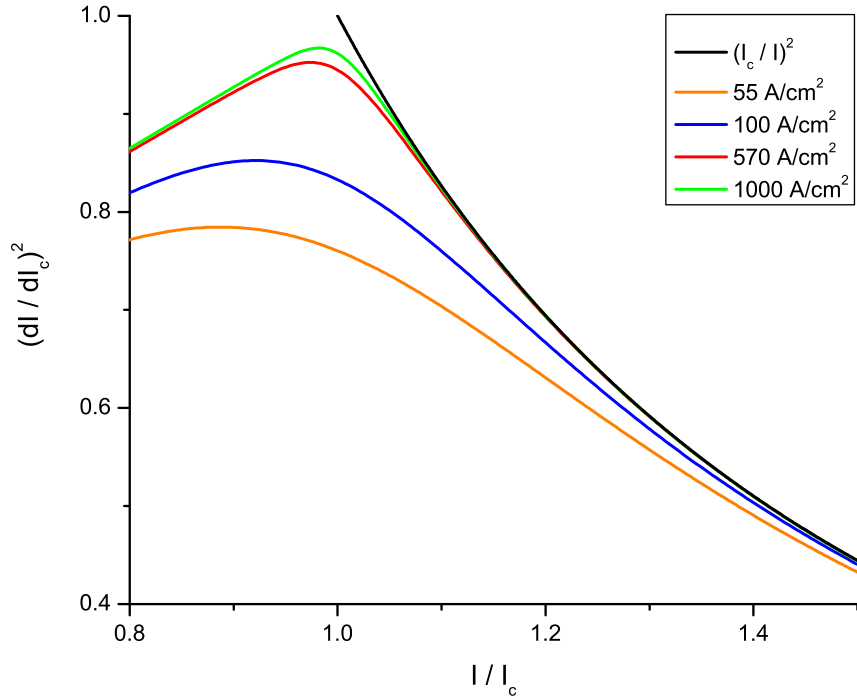
Figure 4.9: The calculated bias dependance of the square of the proportionality constant, $\frac{\partial I}{\partial I_c}$, including thermal fluctuations and plotted as a function of the normalized current through the RSJ at 4.2 K for various critical current density values. The solid black curve is the square of Eqn. 4.10 and is only valid for $I/I_c > 1$.

replaced with $J_c A$ (except for the ratio I_c/I) to give

$$
S_{sens}(T) = \frac{S_{IcN}(T)}{2k_B T} \left(\frac{\beta_c}{C_s} \frac{\Phi_o}{2\pi} \right)^{1/2} J_c^{3/2} \left[1 + 2 \left(\frac{I}{I_c} \right)^2 \right]^{-1}.
\tag{4.12}
$$

S_{sens} will be its largest at $I = I_c$ and is given by

$$
S_{sens}(T) = \frac{S_{IcN}(T)}{6k_B T} \left(\frac{\beta_c}{C_s} \frac{\Phi_o}{2\pi} \right)^{1/2} J_c^{3/2}.
\tag{4.13}
$$

For a given temperature and known value of S_{IcN}, the sensitivity ratio, $S_{sens}(T)$, increases with the current density according to $J_c^{3/2}$. At $T =$

4.2 K, given $\beta_c = 0.3$, $C_s = 45$ fF/μm^2 and $S_{IcN}(4.2K) = 2.2 \cdot 10^{-24}$ (A^2/Hz)(μm/μA)^2 [35] we plot, in Fig. 4.8a, S_{sens} as a function of the current density for $I = I_c$. We see that over an order of magnitude in sensitivity is achieved when increasing the designed critical current density by an order of magnitude from 55 A/cm^2 to 570 A/cm^2.

Calculation of S_{sens} at $I = I_c$ using the I-V expressions which includes thermal fluctuations (Eqn. 1.8), yields a result similar to Eqn. 4.13, shown as the blue curve in Fig. 4.8a. Expressing Eqn. 4.8 in terms of its frequency dependence assuming a $1/f$ dependence of the critical current fluctuations, the following can be written

$$\tilde{S}_{RSJ}(f) = 1 + \frac{S_{sens}(4.2K) \cdot 1\text{Hz}}{f}. \qquad (4.14)$$

Fig. 4.8b plots the above expression for three values of current density at 4.2 K and biased at $I = I_c$. For low J_c at $I = I_c$, thermal fluctuations reduces S_{sens} from the ideal case, but for $I \gg I_c$ the proportionality factor, $\frac{\partial I}{\partial I_c}$, is equal to I_c/I and S_{sens} becomes equal the ideal case as shown in Fig. 4.9.

To verify our use of including thermal fluctuation effects to calculate the proportionality factor (Eqn. 4.7), measurements of $\frac{\partial V}{\partial I_c}$ in an RSJ device having $J_c = 55$ A/cm^2 and $\beta_c = 0.07$ were performed by measuring the voltage as a function of applied magnetic field for a constant current then calculating the derivative. This derivative calculation was repeated at many different current values. The resultant derivative as a function of current while at 1.35 K and a magnetic field of 5 Gauss is shown in Fig. 4.10 and follows the expected dependence (solid line) for thermal fluctuations.

4.1.4 Current Noise in Unshunted Josephson Junctions

In unshunted Josephson junctions biased above the gap voltage, V_g, the critical current fluctuations are negligible and resistance fluctuations in the junction barrier dominate. Here, the total noise from the unshunted JJ is considered to be composed of shot noise, $S_{shot} = 2eI$, and the current noise due to the resistance fluctuations, S_{rJ}, so that the sum of the two noise sources is written as $S_{JJ} = S_{shot} + S_{rJ}$.

For a constant bias the resistance fluctuations generate voltage fluctuations according to $(\partial V)^2 = I^2(\partial R)^2$. Due to the proportionality of the current and voltage above the gap voltage, which follows $V = IR_N$, and a constant $I_c R_N$ product, we can express the fluctuations in the current at a particular bias
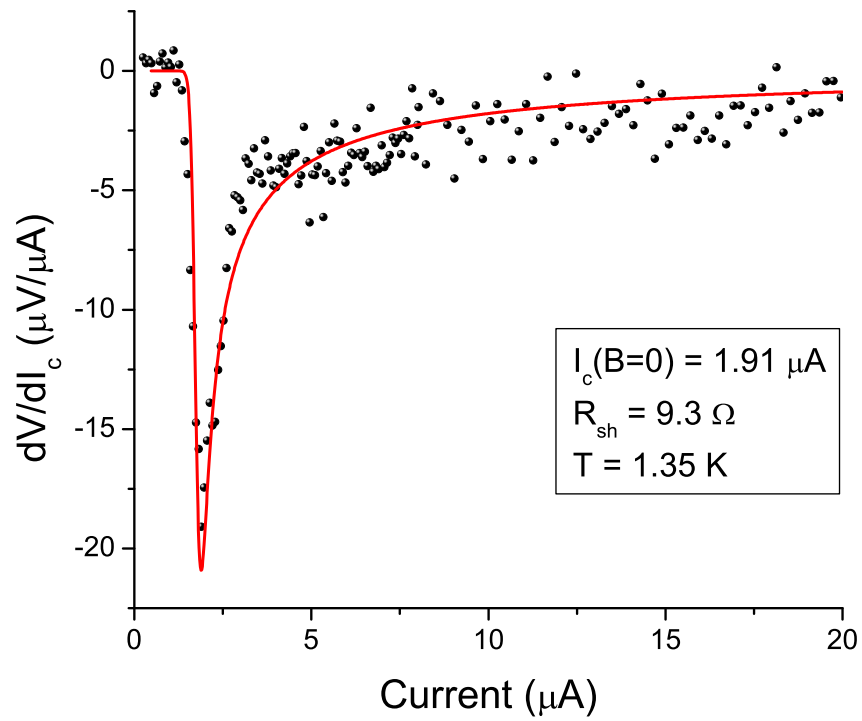
Figure 4.10: Data of the voltage derivative with critical current at 1.35 K for a 3.3 μm^2 shunted junction ($J_c = 55$ A/cm^2) at 5 Gauss. The solid red line is the calculated derivative including thermal fluctuation effects.

point as $(\partial I)^2 = (\partial V)^2/R_N^2$, which allows us to write

$$\frac{(\partial R)^2}{R_N^2} = \frac{(\partial I)^2}{I^2}. \tag{4.15}$$

Using the cyclic relation (Eqn. 4.7) and $V_g \simeq I_c R_N$, it is easy to show that

$$\left(\frac{\partial I}{\partial I_c}\right)_V^2 = \left(\frac{I}{I_c}\right)^2. \tag{4.16}$$

The critical current fluctuations, S_{Ic}, are then inferred from the measured current fluctuations, S_{rJ}, using the expression $S_{rJ} = S_{Ic}\left(\frac{\partial I}{\partial I_c}\right)_V^2$ so that we can write the total noise in the JJ as

$$S_{JJ} = S_{shot} + S_{Ic}\left(\frac{I}{I_c}\right)^2, \tag{4.17}$$

From this analysis, the level of spectral current noise originating from $1/f$ resistance fluctuations should then scale with the current through the junction, I, which we will now denote as I_d.

4.2   Results and Analysis

4.2.1   Analysis of Current Noise

Analysis of the spectral current noise from the measurement requires consideration of the noise contributions from the bridge circuit and the room temperature electronics in order to extract out the noise from RSJ or unshunted Josephson junction. This requires knowledge of the expected spectral dependence of the individual components of the circuit and allows for comparison with the total noise measured.

A simplified diagram of the bridge circuit is shown in Fig. 4.11. Ideally, the total noise should consist of the dc-SQUID magnetometer background noise (S_{sq}), background noise from the room temperature electronics - voltage source (S_{sr}) and bias resistors (S_b), the Johnson noise of the "upper" bridge resistors (S_1), a portion of the Johnson noise from the balancing resistor (S_{bal}), and a portion of the noise from either the RSJ (S_{RSJ}) or unshunted junction (S_{JJ}) device, which we designate both as S_d. The total noise measured by the SQUID detector will then depend upon the dynamic resistance, R_d, of the junction device due to the current division in the circuit, so that the total
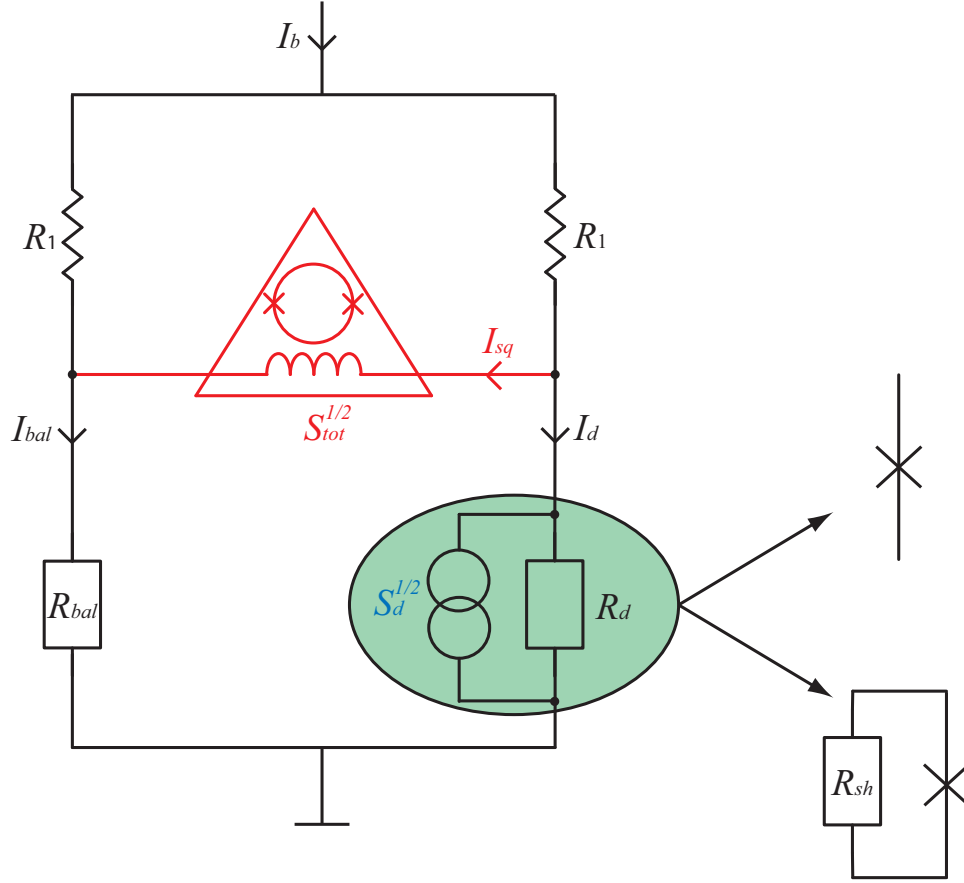
Figure 4.11: Wheatstone bridge circuit diagram excluding the room temperature electronics and filtering elements. The major contributing elements of the total measured noise, S_{tot}, are shown.

noise is given by

$$S_{tot} = S_{sq} + S_1 + \kappa^2 \left(S_{sr} + S_b \right) + \kappa_{bal}^2 \cdot S_{bal} + \kappa_d^2 \cdot S_d \qquad (4.18)$$

where

$$\kappa = \frac{1}{2} \left| \frac{R_d - R_{bal}}{R_{bal} + R_d} \right| , \kappa_{bal} = \left(\frac{R_{bal}}{R_{bal} + R_d} \right) , \kappa_d = \left(\frac{R_d}{R_{bal} + R_d} \right) \qquad (4.19)$$

is the bridge circuit balance factor, and current division factors for the balance resistor and unshunted JJ or RSJ.

To extract the spectral noise of the unshunted JJ or RSJ device, S_d, from the total noise spectra we simply subtract from the total spectral noise the

known noise sources in the circuit and scale according to the current division factor for S_d, which gives

$$S_d = \frac{1}{\kappa_d^2} \left\{ S_{tot} - \left[S_{sq} + S_1 + \kappa^2 \left(S_{sr} + S_b \right) + \kappa_{bal}^2 \cdot S_{bal} \right] \right\}. \qquad (4.20)$$

The contributions to the total spectral noise measured from the known noise sources in the bridge circuit for frequencies at about 1 kHz can be accounted for at zero bias. At zero bias the junction device is superconducting and S_d does not contribute to the total measured noise. The contributing noise sources at zero bias are the SQUID background noise, S_{sq}, and the frequency independent thermal noise sources, S_1 and S_{bal}, as indicated by the circuit diagram shown as the inset of Fig. 4.12.

The circuit diagram shows the upper bridge resistors, R_1, and the SQUID detector are anchored at 4.2 K and the room temperature electronics have been excluded because their noise contribution is negligible. In Fig. 4.12, the total measured noise at 1 kHz of the bridge circuit, $S_{tot}(1\text{ kHz})$, which was configured to measure a 2 μm sized RSJ having $J_c \sim 570$ A/cm^2, is plotted versus temperature for zero current bias. The scaling of the total noise is linear with temperature, and a fit to the data gives the resistance of R_{bal} being 4.48 ± 0.07 Ω with (4.38 ± 0.00) Ω expected, and a temperature independent offset noise of $(0.48 \pm 0.25) \cdot 10^{-24}$ A^2/Hz with $(0.55 \pm 0.03) \cdot 10^{-24}$ A^2/Hz expected.

As suggested above, extraction of the spectral noise due to the unshunted JJ or RSJ device requires knowledge of the current-voltage characteristic and dynamic resistance. With unshunted JJs, this process is simplified because the amount of current flowing through the JJ at a particular voltage bias point can be accurately calculated for bias points above the gap voltage by knowing the total bias current, I_b, and voltage measured across the junction, V_d, by

$$I_d = I_b - \frac{V_d}{R_{bal}}. \qquad (4.21)$$

For the RSJ device, careful measurement of the current-voltage characteristic (I-V) of the RSJ is performed by current sweeping the bridge circuit and measuring the total bias current in the circuit, the voltage across the RSJ device, and the current through the SQUID detector. From the measurement of the SQUID detector current, I_{sq}, the amount of current passing through the RSJ device is determined from $I_d = I_b/2 - I_{sq}$. The I-V obtained is identical to the I-V of the RSJ device measured independently from the bridge circuit. This method also gives the I-V for the balancing resistor to compare with the measured value of resistance from the isolated balancing resistor.
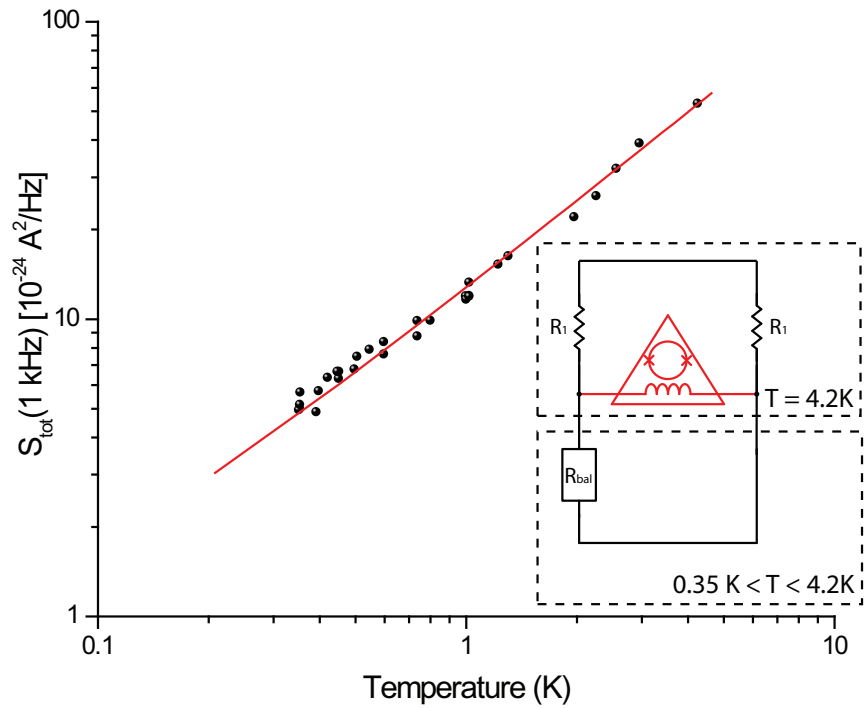
Figure 4.12: Total current noise spectral density, S_{tot}, measured in the bridge circuit at 1 kHz and biased at zero current as a function of temperature and plotted on a log-log scale. The solid red line is a fit to the data which implies a linear scaling with temperature plus a constant term. The inset shows the equivalent circuit for the total noise measured about 1 kHz.
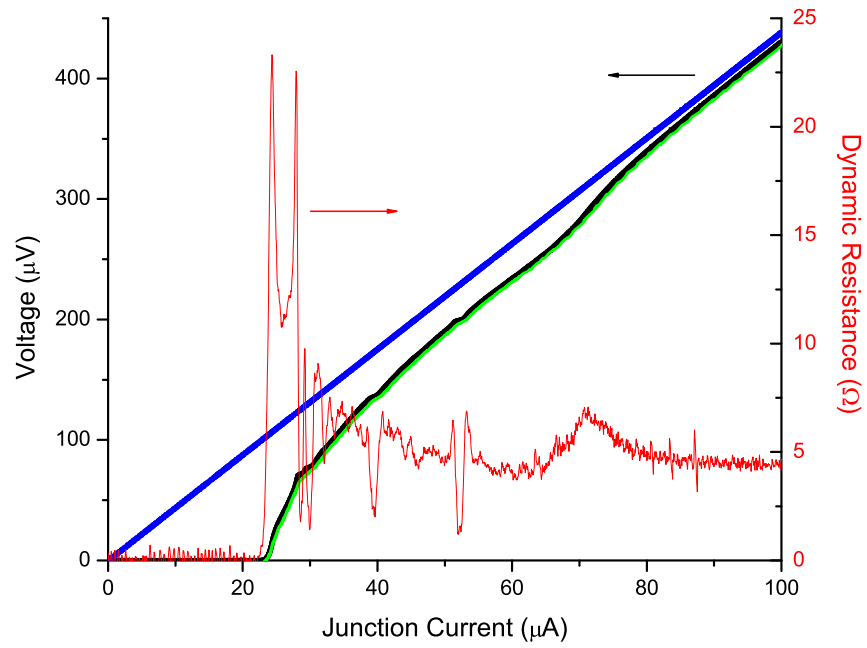
Figure 4.13: Current-voltage characteristics of a 2 μm sized RSJ device (black) and balancing resistor (blue) at 4.2 K. These curves were obtained by calculating I_d and I_{bal} from the measurement of I_b and V_d. The green curve was obtained by directly measuring at 4.2 K the I-V of the 2 μm sized RSJ device alone. The dynamic resistance of the RSJ device is shown as the red curve.

Fig. 4.13 shows the I-V characteristics of a 2 μm sized RSJ device (as in Fig. 4.2) with $J_c \sim$ 570 A/cm^2 having a shunt resistor of 4.4 Ω and a balancing resistor with the same resistance. The dynamic resistance of the RSJ device is also shown in Fig. 4.13. The resonance structure seen in the dynamic resistance curve of Fig. 4.13 is possibly due to the resonant circuit formed by the inductance of the shunt resistor, L_s, and capacitance in the RSJ circuit [38], C_T, which consists of the sum of the junction and resistor capacitances, C_J and C_r. The resonance peak in the I-V near 300 μV roughly corresponds to the voltage that is equal to the fundamental RLC resonance as calculated from an independent estimate [64] of the inductance ($L_s = 2.32$ ph) and capacitance of the RSJ circuit ($C_J = 0.18$ pF, $C_r = 0.436$ pF).

For a resistively shunted junction, the total noise spectra, S_{tot}, (red spectra) of the bridge circuit having a 2 μm junction at 4.2 K is shown in Fig. 4.14 along with the extracted noise portion from the RSJ device, S_d, (blue spectra) which was obtained by using Eqn. 4.20. The black spectral data in Fig. 4.14 is the total noise measured while biased at zero current and is shown for reference. A fit to the total noise spectra or spectral noise from the RSJ while biased at $I_d = I_c$ indicates the data to be composed of low-frequency $1/f$ noise and frequency independent white noise.

Figure 4.15 shows the total spectral noise data, S_{tot}, from the bridge circuit having a 2 μm unshunted junction at 4.2 K (red spectra) while biased at 4.5 mV. The extracted noise portion due to the unshunted JJ, S_d, is shown in Fig. 4.15 as the blue spectra. The black spectral data shown for reference in Fig. 4.15 is the total noise measured while biased at zero current and the solid black line is the expected total noise. Fits to either S_{tot} or S_d, shown respectively as the magenta and cyan solid lines, indicates that the data is composed of low-frequency $1/f$ noise and a frequency independent noise term.

Spectral current noise measured in all unshunted JJs at 4.2 K always exhibited $1/f$ behavior at low frequencies for current bias corresponding to greater than the gap voltage, V_g, between the values of 3.7 mV to 6 mV. All noise spectra measured in the RSJ devices at a current corresponding to the peak in the dynamic resistance (assumed to be equivalent to the critical current) and for temperatures lower than 4.2 K exhibited $1/f$ dependence at low frequencies. Spectral current noise data from the $\sim$570 A/cm^2 RSJ devices at 4.2 K exhibited $1/f$ behavior at low frequencies in initial measurement runs. In later measurement runs of this RSJ device, a Lorentzian peak having the form as in Eqn. 1.19 appeared on top of the $1/f$ spectra at low frequencies. Best fits to the measured spectra from RSJ and unshunted JJ devices exhibiting $1/f$ behavior allowed for extraction of the $1/f$ component of current noise at 1 Hz.
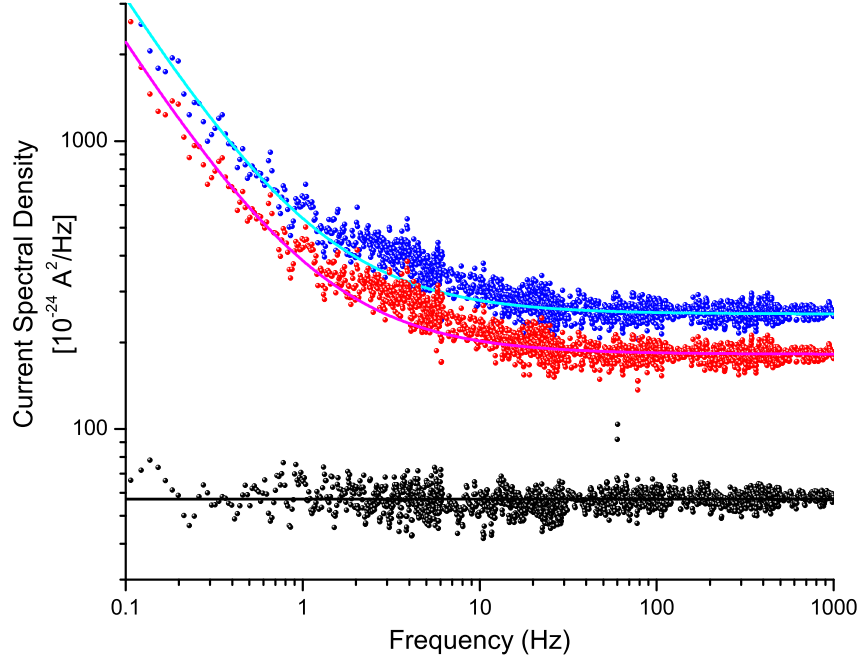
Figure 4.14: Spectral data at $T = 4.2$ K of the total noise, S_{tot}, measured from the Wheatstone bridge circuit having a 2 μm sized RSJ device biased at $I_d = 0$ (black) and $I_d = I_c$ (red). Parameters for the red spectral data are $I_c = 24.7$ μA, $V_d = 12.3$ μV, and $R_d = 23.3$ Ω. The blue spectral data is the noise due to the RSJ while biased at $I_d = I_c$, which was extracted from the total noise. The solid magenta and cyan curves are fits to the spectral data having a $1/f$ and constant noise term, and the solid black line is the expected total noise while biased at zero current.
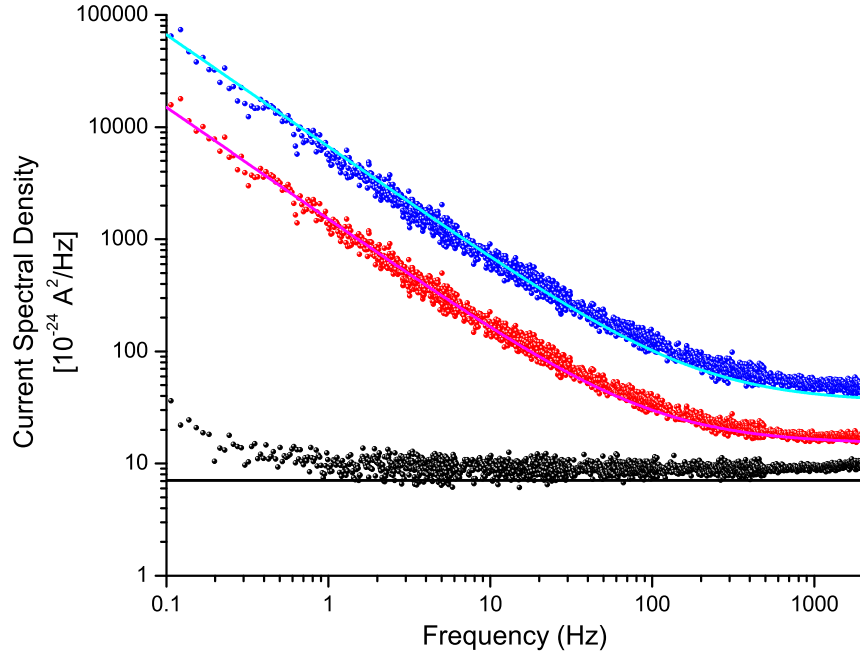
Figure 4.15: Spectral noise data at $T = 4.2$ K of the total noise, S_{tot}, measured in the bridge circuit having a 2 μm sized unshunted Josephson junction (JJ) biased at $I_b = 0$ (black) and $V_d = 4.5$ mV (red). Parameters for the red spectral data are $I_c = 36.1$ μA, $I_d = 110$ μA, and $R_d = 39$ Ω. The spectral noise data due to the JJ, S_d, while biased at $V_g = 4.5$ is shown in blue and was extracted from the total noise. The solid magenta and cyan curves are best fits to S_{tot} and S_d using a $1/f$ and constant noise term. The solid black line is the expected level of background noise at zero bias.

4.2.2 Design Parameter Scaling

Scaling of the current fluctuations at 1 Hz with junction area is observed in the Josephson junction devices. From Eqn. 1.20 and Eqn. 4.16 we know that in unshunted Josephson junctions biased above the gap voltage the current noise due to the critical current fluctuations normalized to the bias current follows

$$\frac{S_{rJ}}{I_d^2} = \frac{S_{Ic}}{I_c^2} = \frac{S_{IcN}}{A}. \tag{4.22}$$

Figure 4.16 shows the current noise spectra from unshunted Josephson junctions, S_d, biased at 3.7 mV at 4.2 K having $J_c = 100$ A/cm^2. The inset plots the $1/f$ component of the current noise $(S_{rJ}(1\text{Hz})/I_d^2)$ at 1 Hz against the junction area, which has a slope whose value is given by S_{IcN}.

As shown in the inset of Fig. 4.16 the solid line through the data indicates the value of the slope, S_{IcN}, at 1 μm^2. S_{IcN} is independent of junction size or critical current density and allows us to compare the level of critical current fluctuations at 1 Hz from various JJ devices, either externally shunted or unshunted, and with other JJ device technologies [4]. In short, comparing the measured S_{IcN} from the various RSJ and JJ devices is a concise way to verify the scaling of the current fluctuations with device size as was demonstrated in Fig. 4.16.

Spectral current noise measurements from both unshunted Nb/AlO$_\text{x}$/Nb Josephson junctions biased above the gap voltage at 4.2 K and in RSJ devices biased near the critical current at 4.2 K were obtained for junction sizes ranging from 1.3 to 10 μm and having current densities of $\sim$50, 100 and $\sim$570 A/cm^2. Data of the normalized critical current fluctuations at 1 Hz of the RSJ and unshunted JJ devices having three different current densities are shown in Fig. 4.17. There is a 10% scatter in the average value from the data in over two orders of magnitude in junction area and one order of magnitude in current density. The average is shown as the solid line through the data.

The normalized value of the critical current fluctuations, S_{I_cN}, which was extracted from the measurements is a factor of $\sim$70 smaller than the empirical literature value [4] of 144 A^2/Hz$\cdot$(μm/μA)^2. These results indicate that the level of normalized critical current fluctuations, S_{IcN}, measured in the RSJ devices biased near their critical current is equal to the normalized critical current fluctuations measured in the unshunted JJ devices at 4.2 K.

4.2.3 Bias Dependence of Current Noise

The spectral noise of the bridge circuit having either the unshunted JJ or RSJ devices was measured at various bias points in order to determine if the
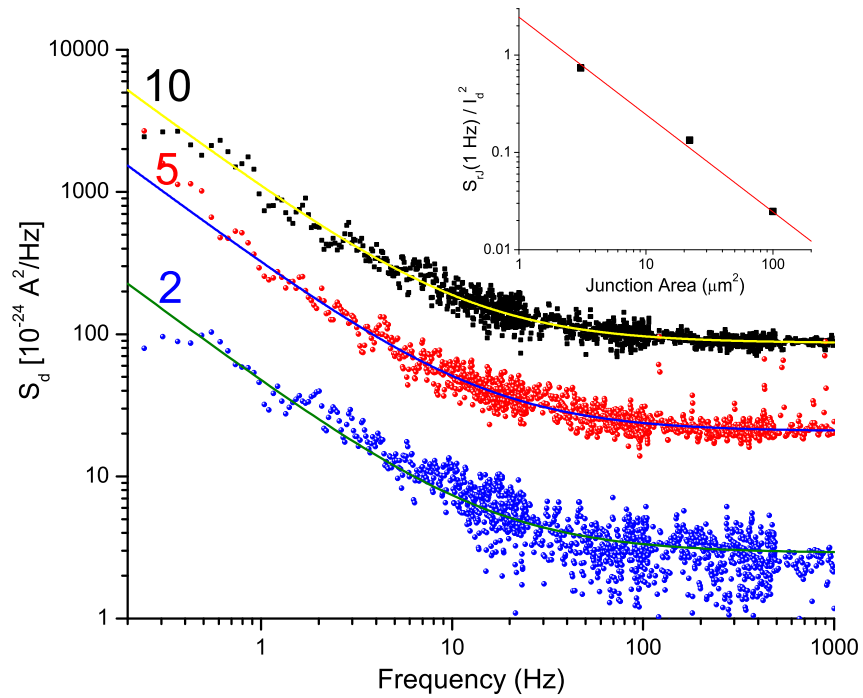
Figure 4.16: Current noise spectra, S_d, of a 2, 5, and 10 μm unshunted JJ at 4.2 K having $J_c = 100$ A/cm^2 and biased at 3.7 mV. The solid curves through the spectral data are fits using $1/f$ and constant noise terms combined. The inset plots the $1/f$ component of the current noise at 1 Hz normalized to the current through the junction, I_d, as a function of junction area, and the red line is a linear fit to the data.
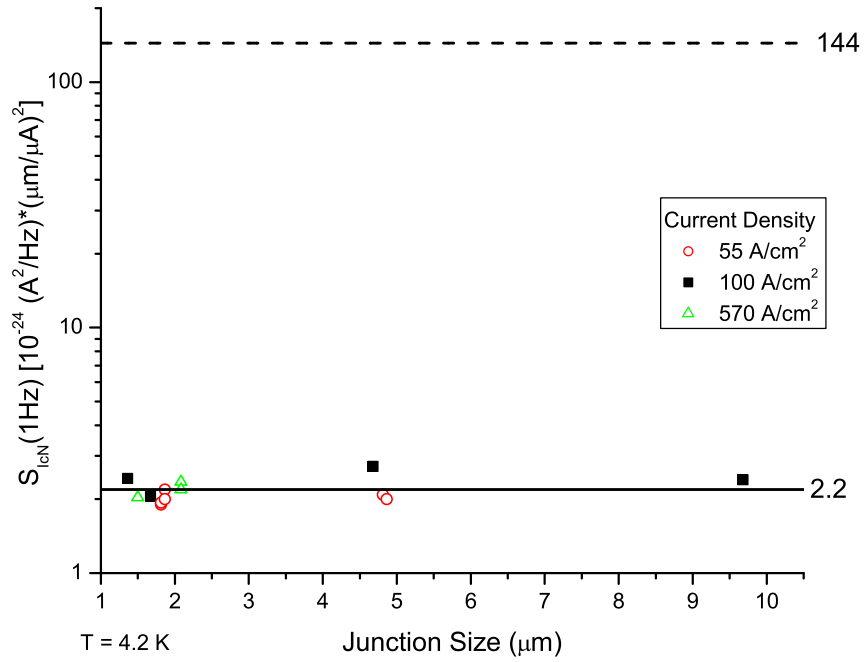
Figure 4.17: Scaling of normalized critical current fluctuations at 1 Hz, $S_{IcN}(1\text{Hz})$, with junction size measured from various RSJ and unshunted JJ devices at 4.2 K. The solid line through the data is the average of the data set, which has a scatter of about 10%. The dashed line above the data is the value of S_{IcN} obtained from ref. [4].
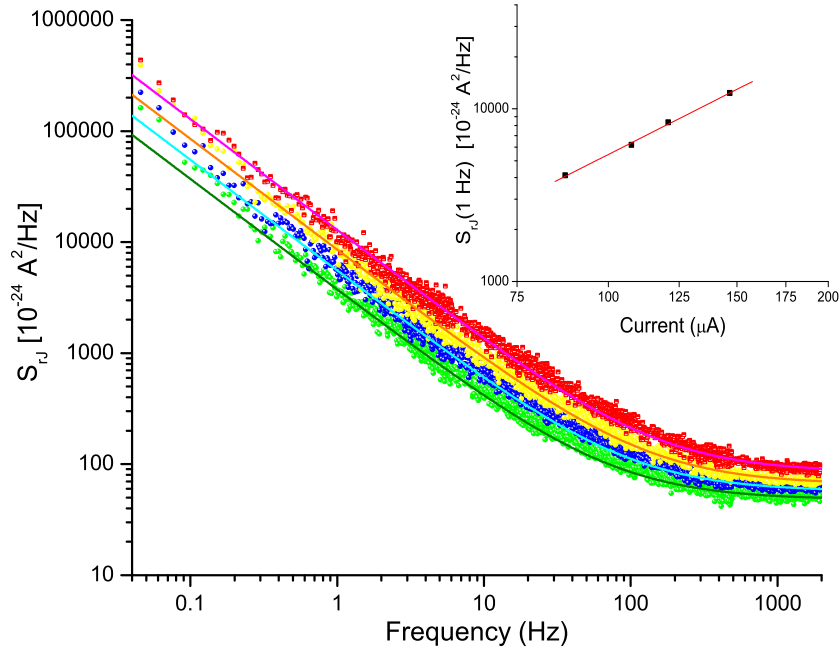
Figure 4.18: Spectral current noise from a 2 μm size $\sim$570 A/cm^2 unshunted JJ, S_d, biased at 3.7 (green), 4.5 (blue), 5 (yellow) and 6 mV (red) at 4.2 K. The solid curves are fits to the data using a $1/f$ term and constant noise term. The inset plots the $1/f$ component of the current noise at 1 Hz as a function of the current through the junction and the red line is a linear fit to the data, which gives a value of 2 for the slope.

bias dependence of the low frequency component of the current noise is related to the expected bias dependence of current fluctuations. Fig. 4.18 plots S_d from a 2 μm sized unshunted Josephson junction at 4.2 K showing how the $1/f$ noise increases with current bias while biased above the gap voltage. The colored spectral data are for bias points of 3.7 (green), 4.5 (blue), 5 (yellow) and 6 mV (red). The inset in Fig. 4.18 plots the $1/f$ component of S_d as a function of current through the junction on a log-log scale. The slope of 2 from the fit to the data in the inset verifies for an unshunted JJ that the $1/f$ noise scales with the bias current as expected.

In an RSJ device while biased at the critical current, the level of the $1/f$ component of the current noise at 1 Hz is nearly equal to the critical current fluctuations due to thermal fluctuations. For current noise measured at points

Figure 4.19: Total current noise measured in the bridge circuit from a 2 μm sized RSJ device having $J_c = 42$ A/cm^2 biased at $1.03I_c$ (red) and $1.33I_c$ (green) at 4.2 K. The solid curves through the data are fits indicating a combined $1/f$ noise term and constant noise term in the spectra. The black spectral data is the total spectral current noise data measured at zero bias current.
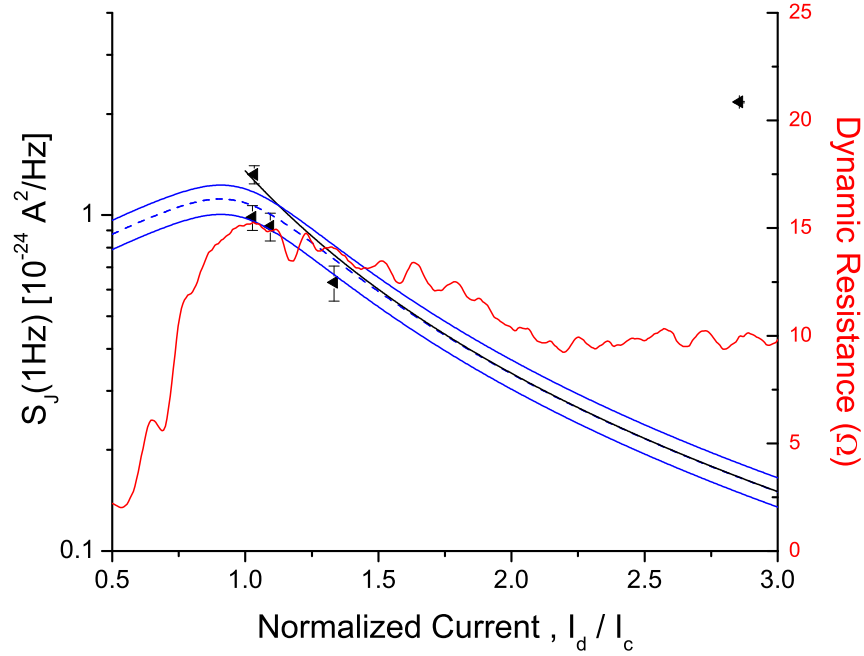
Figure 4.20: The $1/f$ component of the current noise at 1 Hz and 4.2 K as a function of the current, I_d, in a 2 μm size RSJ device having $J_c = 42$ A/cm^2. The solid black line is Eqn. 4.5 calculated using Eqn. 4.10 with $S_{IcN} = 2.2 \cdot 10^{-24}$ A^2/Hz$(\mu$m$/\mu$A$)^2$, $I_c = 1.46$ μA and $A = 3.47$ μm^2. The dashed blue line is the same calculation but including the effects of thermal fluctuations. The solid blue lines above and below the blue dashed line indicate one standard deviation in each direction.

above the critical current, the current noise should scale inversely with the current through the junction according to Eqn. 4.10. Fig. 4.19 shows the total current noise spectra from the bridge circuit with a 2 μm sized RSJ device having $J_c = 42$ A/cm^2 for two bias points above the critical current.

Fig. 4.20 plots the $1/f$ component of the current noise spectra of a 2 μm sized RSJ device having $J_c = 42$ A/cm^2 as a function of normalized current through the device. The $1/f$ noise follows the calculated current bias dependence of current noise, which includes thermal fluctuations, at least up to about $1.33I_c$. Above this bias, the $1/f$ component of the spectral noise from the RSJ increases and cannot be explained by heating effects, which are negligible at 4.2 K for this device. The same data from Fig. 4.20 is plotted against the voltage across the RSJ device in Fig. 4.21. The data shows that

65
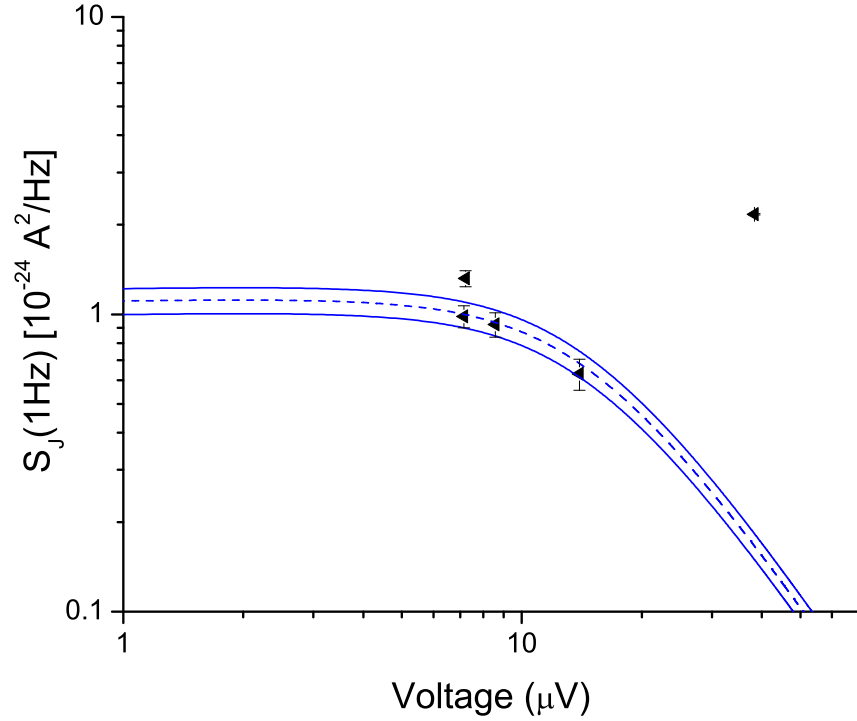
Figure 4.21: The $1/f$ component of the current noise at 1 Hz and 4.2 K as a function of the voltage, I_d, in a 2 μm size RSJ device having $J_c = 42$ A/cm^2. The dashed blue line is Eqn. 4.5 calculated to include thermal fluctuations and using Eqn. 4.10 with $S_{IcN} = 2.2 \cdot 10^{-24}$ A^2/Hz$(\mu$m$/\mu$A$)^2$, $I_c = 1.46$ μA and $A = 3.47$ μm^2. The solid blue lines above and below the blue dashed line indicate one standard deviation in each direction.
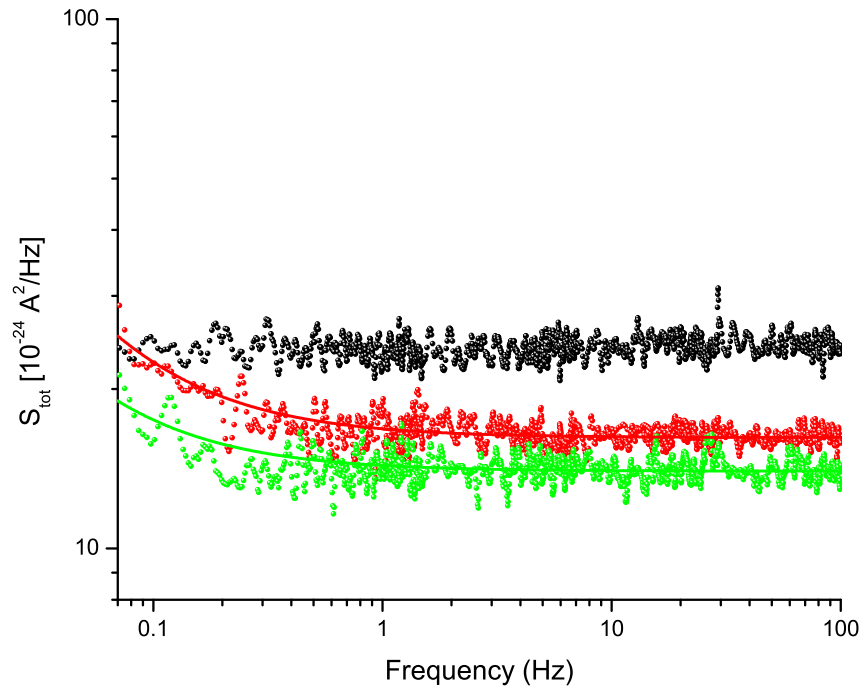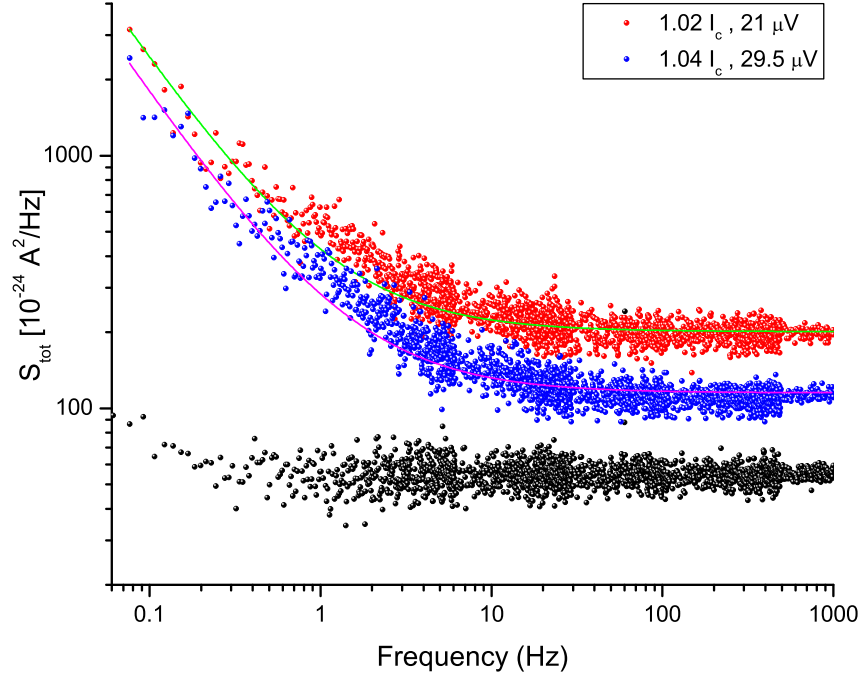
Figure 4.22: Total current noise measured in the bridge circuit from a 2 μm sized RSJ having $J_c \sim 570$ A/cm^2 biased at $1.02 \cdot I_c$ (red) and $1.04 \cdot I_c$ (blue) at 4.2 K. The solid curves through the data are fits indicating a combined $1/f$ noise term and constant noise term in the spectra. The black spectral data is the total spectral current noise data measured at zero bias current. The dynamic resistance at 4.2 K and 1.25 K is plotted for reference.

above roughly 20 μV, the $1/f$ component of the current noise begins to deviate from the expected level of noise (dashed blue line).

In the high current density devices with $J_c = \sim 570$ A/cm^2, Fig. 4.22 shows the total current noise spectra from the bridge circuit with a 2 μm sized device for two bias points near the critical current ($I_c = 24.5$ μA). In this device, the value of the $1/f$ component at 4.2 K and 1.25 K (black and blue symbols), as shown in Fig. 4.23, is consistent with the expected level of current noise (black and blue dashed line) due to critical current fluctuations up to $1.08 \cdot I_c$ and $1.03 \cdot I_c$, respectively. The expected levels of current noise for 4.2 K and 1.25 K were calculated from Eqn. 4.10 using $S_{IcN}(4.2K) = 2.2 \cdot 10^{-24}$ A^2/Hz$(\mu$m$/\mu$A$)^2$ and $S_{IcN}(4.2K) = 0.65 \cdot 10^{-24}$ A^2/Hz$(\mu$m$/\mu$A$)^2$ - the observed temperature dependence of S_{IcN} for $T < 4.2$ K is discussed below in §4.2.4. Above these

67
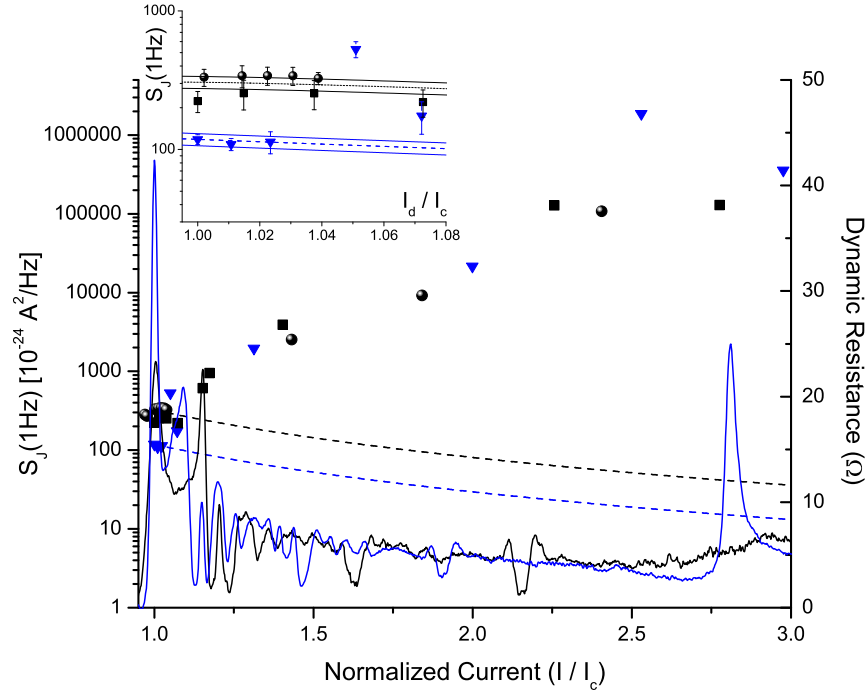
Figure 4.23: The current noise measured from a 2 μm size $\sim$570 A/cm^2 RSJ at 1 Hz for 4.2 K (black circles and squares) and 1.25 K (blue triangles) as a function of current through the device. The dashed lines are Eqn. 4.10 with $S_{IcN}(4.2K) = 2.2{\cdot}10^{-24}$ A^2/Hz$(\mu$m$/\mu$A$)^2$, $I_c(4.2K) = 24.5$ μA, $S_{IcN}(1.25K) = 0.65 \cdot 10^{-24}$ A^2/Hz$(\mu$m$/\mu$A$)^2$, $I_c(1.25K) = 26.9$ μA and $A = 4$ μm^2. The solid black and cyan curves are the dynamic resistance of the device at, respectively 4.2 K and 1.25 K. The inset shows the same data over a smaller range of current near the critical current. The dashed lines are the same as described above and the solid lines above and below the dashed lines indicate one standard deviation in each direction.

68
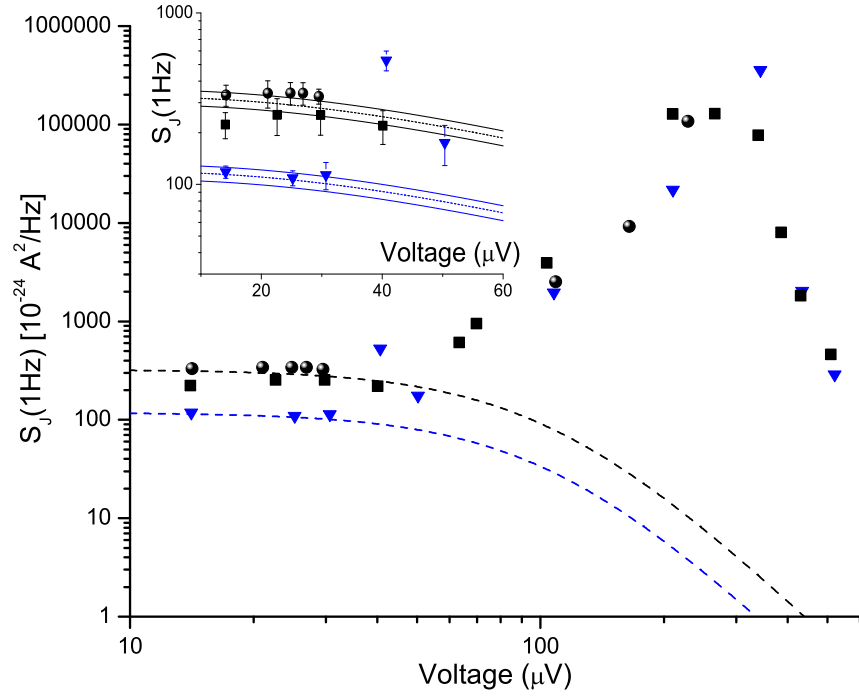
Figure 4.24: The current noise measured from a 2 μm size $\sim$570 A/cm^2 RSJ at 1 Hz for 4.2 K (black circles and squares) and 1.25 K (blue triangles) as a function of the voltage across the device. The dashed lines are Eqn. 4.10 with $S_{IcN}(4.2K) = 2.2 \cdot 10^{-24}$ A^2/Hz(μm/μA)^2, $I_c(4.2K) = 24.5$ μA, $S_{IcN}(1.25K) = 0.65 \cdot 10^{-24}$ A^2/Hz(μm/μA)^2, $I_c(1.25K) = 26.9$ μA and $A = 4$ μm^2. The solid black and blue lines are the expected current noise at 1 kHz for, respectively, 4.2 K and 1.25 K. The inset shows the same data over a smaller range of voltage near the critical current. The dashed lines are the same as described above and the solid lines above and below the dashed lines indicate one standard deviation in each direction.

69

bias points the $1/f$ noise begins to deviate from Eqn. 4.10 and increases with bias current.

The data in Figs. 4.23 and 4.21 represented as black circles and squares are, respectively, measurements of the 2 μm sized RSJ device corresponding to two separate measurement runs differing by about 6 months with thermal cycling to room temperature. The black squares and blue triangles correspond to the same measurement run.

In Fig. 4.24, the current noise data from Fig. 4.23 is plotted against the voltage across the RSJ, and includes data over a larger range of bias in order to illustrate two points. First, the data shows that the $1/f$ noise is consistent with the expected bias dependence of the critical current fluctuations at least up to 40 μV at 4.2 K and 30 μV at 1.25 K. For clarity of this point, the inset shows the same data but corresponding to a smaller range of voltage bias near the critical current. Second, we see that the level of $1/f$ noise increases until about 300 μV at which point it steadily decreases for at least up to 600 μV. This appears to correspond to a peak in the dynamic resistance seen in Fig. 4.13 at nearly the same point in voltage.

The resonant structure seen in the I-V characteristics of Fig. 4.13 is also observed in other low and high J_c RSJ devices and are shown in Fig. 4.25, where Fig. 4.25b is I-V data at 1.3 K of the 2 μm sized RSJ device having $J_c = 42$ A/cm^2, which was discussed above (see Fig. 4.20). It is suggested, then, that the increase in the $1/f$ component of the current noise measured in the low and high J_c RSJ devices previously discussed above may be related to the resonant structure in the I-V due to the RLC circuit formed by the RSJ device [38].

4.2.4   Temperature Dependence of Critical Current Fluctuations

A temperature series measurement of the current spectral density from 4.2 K to 410 mK was performed with two 4 μm^2 RSJ devices ($R_{sh} = 4.4$ Ω) having $J_c \sim 570$ A/cm^2. The devices were biased near the critical current for all measurements of the noise spectra. Following the analysis previously described in §4.2.1, the $1/f$ component of the current noise from the RSJ device, $S_J(1Hz)$, was extracted and converted to a normalized value of critical current fluctuations, $S_{IcN}(T)$, for each temperature at which the spectral noise was measured. For measurements of the current spectral density at temperatures below 1.2 K, the $1/f$ component of the spectral noise was extracted from spectra that were obtained while current biased at either $1.03I_c$ or $1.06I_c$, where I_c is taken to be the peak in the measured dynamic resistance for a
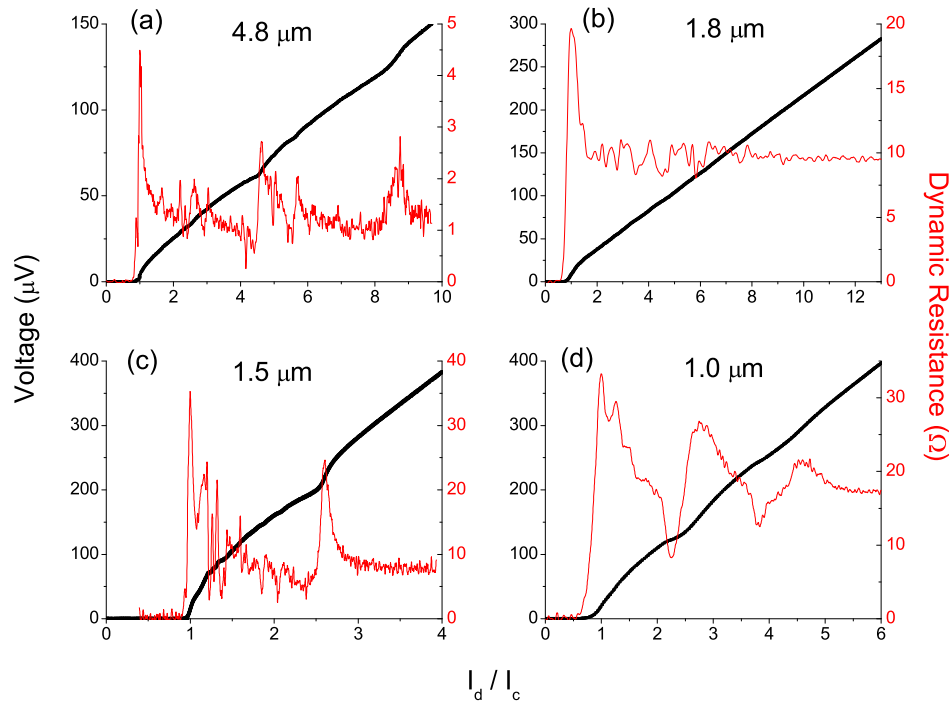
Figure 4.25: Measured current-voltage characteristics and their respective dynamic resistance curves of various high and low J_c RSJ devices. The horizontal scale is the normalized current, I_d/I_c. The vertical scales on the left and right of the graphs are the voltage and dynamic resistance, respectively. Parameters of the RSJ devices shown are (a) $(4.8 \ \mu m)^2$, $I_c = 12.3 \ \mu A$, $R = 1.25 \ \Omega$, $T = 4.2$ K (b) $(1.8 \ \mu m)^2$, $I_c = 2.3 \ \mu A$, $R = 9.6 \ \Omega$, $T = 1.3$ K (c) $(1.5 \ \mu m)^2$, $I_c = 12.7 \ \mu A$, $R = 7.8 \ \Omega$, $T = 4.2$ K (d) $(1.0 \ \mu m)^2$, $I_c = 3.9 \ \mu A$, $R = 17.2 \ \Omega$, $T = 4.2$ K.
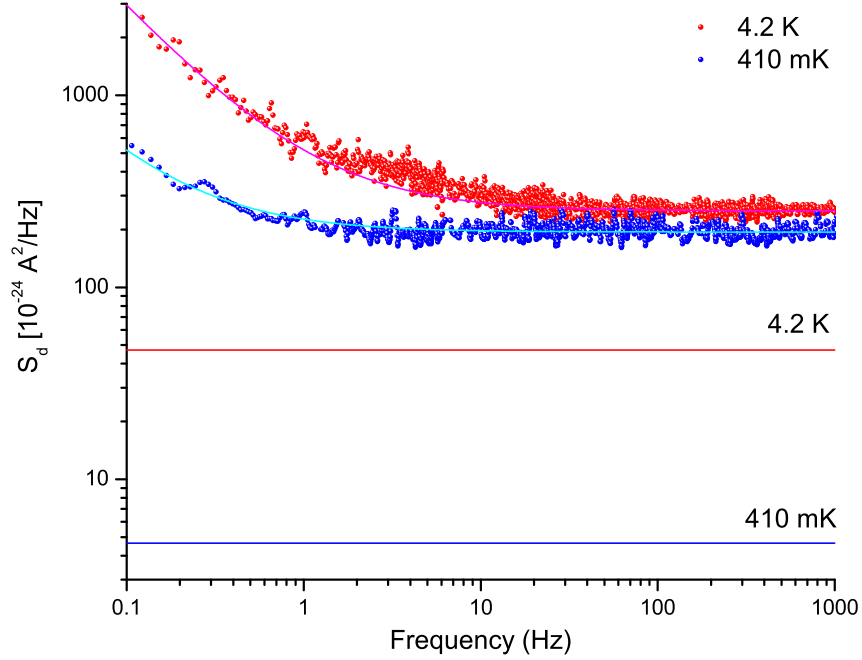
Figure 4.26: Measured current spectral density from the RSJ device having $J_c \sim 570$ A/cm^2 at bath temperatures 4.2 K and 410 mK and biased at $I_d/I_c = 1.03$. The solid magenta and cyan lines through the spectra are fits to the data at 4.2 K and 410 mK. The solid red and blue lines below the spectra are the expected total white noise at 1 kHz.

given temperature. For bath temperatures below 600 mK and biased near the critical current as described above, the temperature of the RSJ device was calibrated using the electron bath heating curves discussed in §4.1.2. At the lowest bath temperature of $T = 370$ mK while biased at $1.06I_c$ having about 1 nW power dissipated in the resistor of the RSJ device studied here, the calibrated temperature was 40 mK above the bath temperature. For other bias points and bath temperatures greater than 370 mK, the calibration in the temperature of the RSJ device was less than 40 mK.

In Fig. 4.26, spectral current noise measurements from 0.1 Hz to 1 kHz of an externally shunted ($R_{sh} = 4.4$ Ω) 4 μm^2 junction at 4.2 K and 410 mK biased near the critical current is shown. While biased near I_c an increased level of white noise is observed, which does not scale linearly with temperature as would be expected for Johnson noise and can not be accounted for by hot electron heating of the shunt resistor or solely from down-converted noise from
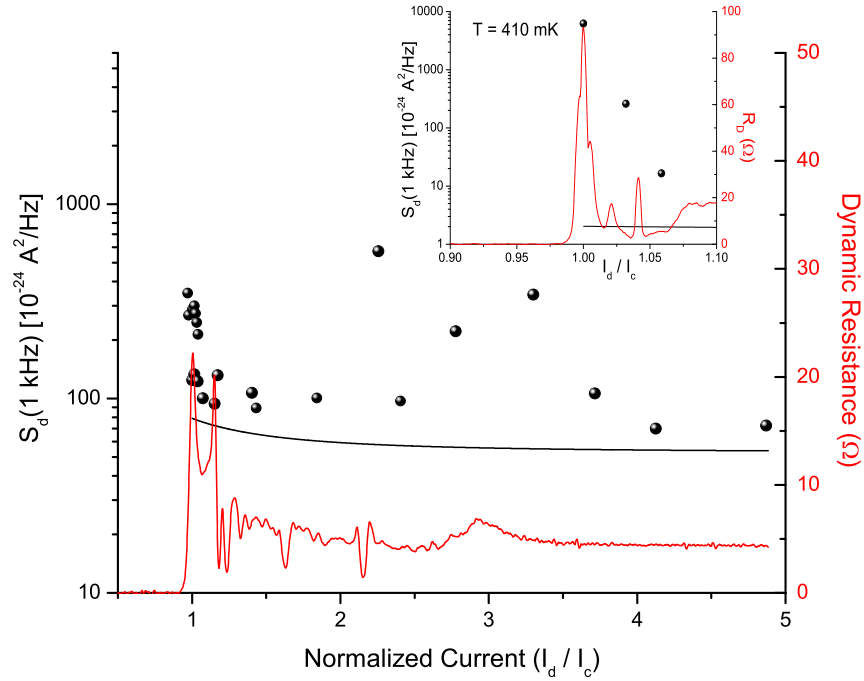
Figure 4.27: Current bias dependence on the spectral current noise at 1 kHz at 4.2 K from a 2 μm RSJ device. The black circles are the data and the solid black line is the expected noise at 1 kHz using Eqn. 1.18. The inset shows similar data at 410 mK. The red curves are the dynamic resistance of the junction as a function of bias current.

the radiation at the Josephson oscillation frequency [38, 39, 65].

Fig. 4.27 shows the level of spectral white noise measured about 1 kHz in the 2 μm RSJ device as a function of bias current at 4.2 K and 410 mK. The data show that the level of measured white noise considerably deviates from the expected level of total current noise at 1 kHz (Eqn. 1.18). It was shown previously that the expected $1/f$ component of the current noise was consistent over a small region of bias current with the measured data while the observed level of white noise at 1 kHz is shown to be inconsistent with the expected white noise level. This suggests that the $1/f$ component of the spectral noise is not correlated with the bias effects on the white noise at least up to the bias points discussed in §4.2.3 for this device.

The normalized critical current fluctuations at 1 Hz calculated from the
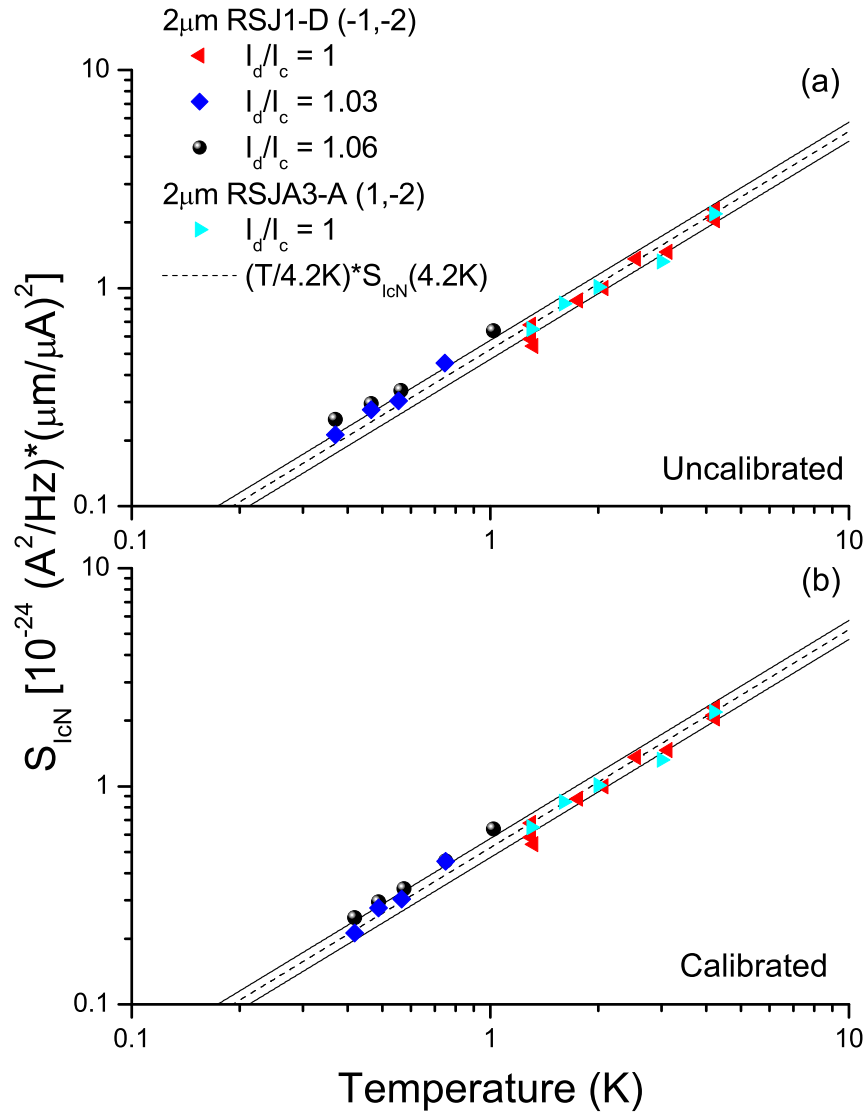
Figure 4.28: The normalized current spectral density at 1 Hz of two RSJ devices each having an area of 4 μm^2 plotted against an (a) uncalibrated and (b) calibrated temperature scale. The dashed line shown in (a) and (b) is a linear fit to the data in (b) and has a slope of $S_{IcN}(4.2K, 1Hz) \cdot (1/4.2K)$. The solid lines above and below the dashed line indicate one standard deviation in each direction.

$1/f$ component of the current noise is $S_{IcN} = 2.2 \cdot 10^{-24}$ A^2/Hz $\cdot$ (μm/μA)^2 at 4.2 K. Cooling the RSJ device to 410 mK the measured spectra, as seen in Fig. 4.26, exhibited low-frequency $1/f$ behavior while biased near the critical current. The level of the $1/f$ component of the noise was observed to decrease at this temperature and a value of normalized critical current fluctuations of $S_{IcN} = 0.23 \cdot 10^{-24}$ (A^2/Hz) $\cdot$ (μm/μA)^2 at 410 mK is obtained. In Figs. 4.28a and b, the normalized critical current fluctuation data, S_{IcN}, obtained from spectral measurements at various temperatures is plotted. Fig. 4.28a plots S_{IcN} on an uncalibrated temperature scale and Fig. 4.28b plots S_{IcN} on a calibrated temperature scale following the procedure described above. The data in Fig. 4.28b is observed to follow a linear scaling with temperature such that the following relation can be defined

$$S_{IcN}(T) = S_{IcN}(4.2K) \cdot \frac{T}{4.2K}. \tag{4.23}$$

The slope extracted from the fit to the data in Fig. 4.28b is $S_{IcN}(4.2\text{K}) \cdot 1/4.2$ K $= 0.52 \cdot 10^{-24}$ A^2/Hz $\cdot$ (μm/μA)$^2 \cdot$K^{-1}.

The scaling of the critical current fluctuations with area and the linear temperature dependence of the critical current fluctuations in Nb/AlO$_x$/Nb Josephson junctions demonstrated here suggests that the prevalent model of conductance fluctuations [41, 43] in the AlO$_x$ barrier remains a likely model to explain the mechanism of critical current fluctuations in Josephson junctions. Reconciling the differences between the mechanism of the linear temperature scaling of critical current fluctuations observed from our results with that of other results [27, 28, 42] remains to be demonstrated.

The results demonstrated here suggest that if a linear temperature scaling of the critical current fluctuations in Josephson junctions persists down to 10 mK in Nb/AlO$_x$/Nb based qubits, then a reconsideration of the level of critical current fluctuations as a potential source of dephasing noise must be made over previous assumptions of the dephasing effects of critical current fluctuations at lower temperatures [4].

Chapter 5

Closing Arguments

5.1 Summary

We have presented in this thesis methods for measuring and characterizing properties of Josephson junctions that determine some of the limiting factors of coherence of the quantum mechanical states of an rf-SQUID qubit. Measurements of the subgap quasiparticle leakage current and critical current fluctuations in $Nb/AlO_x/Nb$ Josephson junctions fabricated at Stony Brook University have been shown to demonstrate low sub-gap leakage quality and low critical current fluctuations. The low leakage current of the junctions in the sub-1K temperature region indicates low or negligible intrinsic quasiparticle damping in the rf-SQUID qubit compared to other sources of decoherence [19, 66]. The low critical current fluctuations measured at 4.2 K and for temperatures down to 0.4 K, which follows a linear temperature dependence, suggests a dephasing time orders of magnitude longer than what is observed in our rf-SQUID qubits [29] at their operating temperature near 20 mK. This suggests that neither intrinsic quasiparticle damping nor critical current fluctuations in the Josephson junctions should be a limiting factor in the dephasing time of $Nb/AlO_x/Nb$ based rf-SQUID qubits fabricated at Stony Brook.

Other sources of noise, such as flux noise, may be a more dominant source of decoherence. A study by Nakamura et al. [19] found that $1/f$ flux noise, observed from studying the spin-echo dephasing rates, was of the order $(10^{-6}\Phi_o)^2/Hz$ and was the dominant source of decoherence in $Al/AlO_x/Al$ flux qubits. Di Vincenzo et al. have proposed that the flux noise is generated by electron orbital magnetic moments in defect states that are randomly occupied for some given lifetime before escaping[18]. Their recent simulations of a microscopic theory for flux noise attempts to corroborate the above findings

for flux noise observed by Nakamura et al.

Our results of the linear temperature scaling of critical current fluctuations in RSJ devices are similar to the findings of a study of conductance fluctuations in $Al/AlO_x/Al$ Josephson junctions [28]. The significant differences between our results being that we did not suppress the supercurrent in the electrodes of our devices and we are directly measuring the critical current fluctuations of the Josephson junction. A recent model [42] that suggested the linear temperature scaling of critical current fluctuations demonstrated in $Al/AlO_x/Al$ Josephson junctions with the supercurrent in the leads suppressed with a magnetic field [28] originates from conductance fluctuations in the barrier. In addition, critical current fluctuations following a quadratic scaling with temperature observed in $Nb/NbO_x/PbIn$ Josephson junctions where their electrodes are superconducting is suggested by Faoro et al. as originating from electron tunneling across the barrier between charge traps at the superconductor-insulator interface [42] of the junction. According to this result our temperature dependence study suggests that charge traps at the superconductor-insulator interface are not a dominant source for causing critical current fluctuations.

5.2   Suggestions for Future Work

The analysis on the measurement of critical current fluctuations in the RSJ devices that have been studied deserves some further discussion. While the level of normalized critical current fluctuations measured at 1 Hz in various RSJ devices biased at the critical current was consistent with that measured in similar unshunted Josephson junctions biased above their gap voltage, the inconsistency between the expected current bias dependence of the critical current fluctuations is troublesome.

The data shown in chapter 4 supports the expected current bias dependence of the fluctuations up to 6 to 10% above the critical current. We suggest that this could be due to an independent current noise source located at the contacts between the AuPd resistor and Nb leads that becomes a dominant noise source above roughly 40 μV as seen in Fig. 4.24. A similarly designed RSJ device could be fabricated having no defined junction. Measurement of the current spectral noise of this device in our bridge circuit would test what current bias dependent noise sources are inherent in this particular design excluding the Josephson junction.

Additionally, as we had suggested in §4.2.3, there is some correlation between the increase in the level of $1/f$ noise and the voltage peaks in the I-V of the RSJ device. As seen in Fig. 4.24 the level of $1/f$ noise begins

to decreases at a bias above roughly 300 μV where one can see a prominent peak in the dynamic resistance. This peak roughly occurs at the fundamental frequency of the RLC circuit resonance ($n = 1$), which is estimated to be at about 275 μV from using the capacitances of the junction and resistor and the inductance of the resistor. By changing the inductance or capacitance of the RLC circuit of the 2 μm RSJ device such that the fundamental resonance frequency is halved would in principle test whether the peaks are indeed sub-harmonic resonances and whether the bias dependence of the level of $1/f$ current noise is related to this circuit resonance structure.

Modifying the capacitance of the resistor by increasing its area while keeping the inductance constant would one simple way to change the RLC resonance. It is straightforward to increase the capacitance of the resistor, thereby decreasing the RLC resonance, by adding a fin with a ground plane to increase the area of the resistor while keeping its resistance and inductance constant. This resistor design would also benefit from a larger volume of metal in that hot electron heating effects would be reduced from the levels observed in the current design.

Bibliography

[1] Daniel Loss and David P. Divincenzo. Quantum computation with quantum dots. *Phys. Rev. A*, 57:120, 1998.

[2] U. Weiss, H. Grabert, and S. Linkwitz. Influence of friction and temperature on coherent quantum tunneling. *JLTP*, 68:213–244, 1987.

[3] A. J. Leggett, S. Charkavarty, A. T. Dorsey, Matthew P. A. Fisher, Anupam Garg, and W. Zwerger. Dynamics of the dissipative 2-state system. *RMP*, 59:1–85, 1987.

[4] D.J. Van Harlingen et al. Decoherence in josephson-junction qubits due to critical-current fluctuations. *PRB*, 70:064517, 2004.

[5] Michael Nielsen and Isaac Chuang. *Quantum Computation and Quantum Information.* Cambridge University Press, Cambridge UK, 2000.

[6] G. J. Dolan. Offset masks for lift-off photoprocessing. *Appl. Phys. Lett.*, 31:337, 1977.

[7] M. Gurvitch, M. A. Washington, and H. A. Huggins. High quality refractory josephson tunnel junctions utilizing thin aluminum layers. *Appl. Phys. Lett.*, 42:472, 1983.

[8] M. Gurvitch, M. A. Washington, and H. A. Huggins. Sub-μm, planarized, Nb/Al-oxide-Nb josephson process for 125 mm wafers developed in partnership with si technology. *Appl. Phys. Lett.*, 59:2609, 1991.

[9] Y. Nakamura, Yu. A. Pashkin, and J. S. Tsai. Coherent control of macroscopic quantum states in a single-cooper-pair box. *Nature*, 398: 786–788, 1999.

[10] Jonathan R Friedman, Vijay Patel, Wei Chen, S. K Tolpygo, and James E. Lukens. Quantum superpostion of distinct macroscopic states. *Nature*, 406:43–46, 2000.

[11] C. H. van der Wal et al. Quantum superposition of macroscopic persistent-current states. *Science*, 290:773–777, 2000.

[12] D. Vion et al. Manipulating the quantum state of an electrical circuit. *Science*, 296:886–889, 2002.

[13] Y. Yu, S. Han, X. Chu, S. Chu, and Z. Wang. Coherent temporal oscillations of macroscopic quantum states in a josephson junction. *Science*, 296:889–892, 2002.

[14] J. M. Martinis, S. Nam, and J. Aumentado. Rabi oscillations in a large josephson-junction qubit. *PRL*, 89(11):117901, 2002.

[15] E. Il'ichev et al. Continuous monitoring of rabi oscillations in a josephson flux qubit. *PRL*, 91(9):097906, 2003.

[16] A. Wallraff et al. Approaching unit visibility for control of a superconducting qubit with dispersive readout. *PRL*, 95(6):060501, 2005.

[17] S. Oh, Katarina Cicak, Jeffrey S. Kline, Mika A. Sillanpää, K. D. Osborn, Jed D. Whittaker, Raymond W. Simmonds, and David P. Pappas. Elimination of two level fluctuators in superconducting quantum bits by an epitaxial tunnel barrier. *PRB*, 74:100502, 2006.

[18] Roger H. Koch, David P. DiVincenzo, and John Clarke. Model for $1/f$ flux noise in squids and qubits. *arXiv:cond-mat/0702025v2*, pages 1–16, May 2007.

[19] F. Yoshihara et al. Decoherence of flux qubits due to $1/f$ flux noise. *Phys. Rev. Lett.*, 97:167001, Oct 2006.

[20] S. X. Li, W. Qiu, M. Matheny, Z. Zhou, and S. Han. Energy relaxation time of an rf squid flux qubit. Applied Superconductivity Conference, 2004.

[21] F. P. Milliken, R. H. Koch, J. R. Kirtley, and J. R. Rozen. *APL*, 85:5941, 2004.

[22] M. A. Gubrud et al. Sub-gap leakage in $Nb/AlO_x/Nb$ and $Al/AlO_x/Al$ josephson junctions. In *IEEE Trans. Appl. Supercond.*, volume 11, pages 1002–1005, 2001.

[23] Robert M. Handy. Electrode effects on aluminum oxide tunnel junctions. *Phys. Rev.*, 126:1968, 1962.

[24] J. V. Gates, M. A. Washington, and M. Gurvitch. Critical current uniformity and stability of Nb/Al-oxide-Nb josephson junctions. *J. Appl. Phys.*, 55:1419, 1984.

[25] S. Oh, K. Cicak, R. McDermott, K. B. Cooper, K. D. Osborn, R. W. Simmonds, M. Steffen, J. M. Martinis, and D. P. Pappas. Low-leakage superconducting tunnel junctions with a single-crystal Al_2O_3 barrier. *Supercond. Sci. Technol.*, 18:1396–1399, 2005.

[26] Micheal Muck, Matthias Korn, C. G. A. Mugford, J. B. Kycia, and John Clarke. Measurements of $1/f$ noise in josephson junctions at zero voltage: Implications for decoherence in superconducting quatum bits. *APL*, 86: 012510, 2005.

[27] F. C. Wellstood, C. Urbina, and John Clarke. Flicker $(1/f)$ noise in the critical current of josephson junctions at $0.09-4.2$ K. *APL*, 85:5296–5298, 2004.

[28] J. Eroms, L. C. van Schaarenburg, E. F. C. Driessen, J. Plantenberg, and K. Huizinga. Low-frequency noise in josephson junctions for superconducting qubits. *APL*, 89:122516, 2006.

[29] Douglas A. Bennett, Luigi Longobardi, Vijay Patel, Wei Chen, and James E. Lukens. rf-squid qubit readout using a fast flux pulse. *Supercond. Sci. Technol.*, 20:445, 2007.

[30] B. D. Josephson. Possible new effects in superconductive tunneling. *Phys. Lett.*, 1:251, 1962.

[31] W. C. Stewart. *Appl. Phys. Lett.*, 12:277, 1968.

[32] D. E. McCumber. *J. Appl. Phys.*, 39:3113, 1968.

[33] Ivanchenko Y. M. and Zil'berman L. A. Destruction of josephson current by fluctuations. *JETP Lett.*, 8:113–115, 1968.

[34] Ambegaokar V. and Halperin B. J. Voltage due to thermal noise in the d.c. josephson effect. *PRL*, 22:1364–1366, 1969.

[35] Vijay Patel, Wei Chen, Shawn Pottorf, and James E. Lukens. A fast turn-around time process for fabrication of qubit circuits. In *IEEE Trans. Appl. Supercond.*, volume 15, pages 117–120, June 2005.

[36] J. B. Johnson. Thermal agitation of electricity in conductors. *Phys. Rev.*, 32(1):97, Jul 1928.

[37] H. Nyquist. Thermal agitation of electric charge in conductors. *Phys. Rev.*, 32(1):110–113, Jul 1928.

[38] R. H. Koch, D. J. Van Harlingen, and J. Clarke. Measurements of quantum noise in resistively shunted josephson-junctions. *PRB*, 26:74, 1982.

[39] K. K. Likharev and V. K. Semenov. *JETP Lett.*, 15:442, 1972.

[40] Richard F. Voss. Noise characteristics of an ideal shunted josephson junction. *Jour. Low Temp. Phys.*, 42:151, 1981.

[41] P. Dutta, P. Dimon, and P. M. Horn. Energy scales for noise processes in metals. *Phys. Rev. Lett.*, 43(9):646–649, Aug 1979.

[42] Lara Faoro and Lev B. Ioffe. Microscopic origin of critical current fluctuations in large, small, and ultra-small area josephson junctions. *Phys. Rev. B*, 75:132505, Apr 2007.

[43] C. T. Rogers and R. A. Buhrman. Nature of single-localized-electron states derived from tunneling measurements. *PRL*, 55:859–862, 1985.

[44] A. I Larkin and Yu. N. Ovchinnikov. Quantum tunneling with dissipation. *JETP Letters*, 37:382–385, Apr 1983.

[45] Richard F. Voss and Richard A. Webb. Macroscopic quantum tunneling in 1-μm nb josephson junction. *Phys. Rev. Lett.*, 47:265, Jul 1981.

[46] E. Dantsker, S. Tanaka, P. Å. Nilsson, R. Kleiner, and J. Clarke. *Appl. Phys. Lett.*, 69:4099, 1996.

[47] A. J. Leggett. In *Les Houches, Session XLVI-Chance and Matter*, pages 395–506. Elsevier, 1987.

[48] Wei Chen, Vijay Patel, and James E. Lukens. Fabrication of high-quality josephson junctions for quantum computation using a self-aligned process. *Microelectronic Engineering*, 73-74:767, 2004.

[49] Wei Chen, Vijay Patel, Sergey K. Tolpygo, Daniel Yohannes, Shawn Pottorf, and James E. Lukens. Development toward high-speed integrated circuits and squid qubits with Nb/AlO$_x$/Nb josephson junctions. In *IEEE Trans. Appl. Supercond.*, volume 13, pages 117–120, June 2003.

[50] Juhani Kurkijarvi. Intrinsic flucuations in a superconducting ring closed with a josephson junction. *PRB*, 6(3):832–835, 1972.

[51] Michel H. Devoret, John M. Martinis, and John Clarke. Measurements of macroscopic quantum tunneling out of the zero-voltage state of a current-biased josephson junction. *Phys. Rev. Lett.*, 55:1908, 1985.

[52] Anupam Garg. Escape-field distribution for escape from a metastable potential well subject to a steadily increasing bias field. *Phys. Rev. B*, 51:15592, 1995.

[53] J. Mannik, S. Li, w. Qiu, W. Chen, V. Patel, S. Han, and J. E. Lukens. Crossover from kramers to phase-diffusion switching in moderately damped josephson junctions. *PRB*, 71:220509, 2005.

[54] C. J. Lobb A. T. Johnson and M. Tinkham. Effect of leads and energy gap upon the retrapping current of josephson junctions. *Phys. Rev. Lett.*, 65:1263, 1990.

[55] C. Nappi, R. Christiano, L. Frunzio, S. Pagano, and M. P. Lisitskii. On the magnetic field dependence of the critical current in small irregular polygonal josephson junctions. *J. Appl. Phys.*, 80:3401, 1996.

[56] B. N. Taylor and E. Burstein. Excess currents in electron tunneling between superconductors. *Phys. Rev. Lett.*, 10:1963, 1963.

[57] K. Rabenstein, V. A. Sverdlov, and D. V. Averin. Qubit decoherence by gaussian low-frequency noise. *JETP Letters*, 79:646–649, 2004.

[58] Bonaventura Savo, Frederick C. Wellstood, and John Clarke. Low-frequency excess noise in Nb-Al_2O_3-Nb of josephson tunnel junctions. *APL*, 50:1757–1759, 1987.

[59] V. Foglietti, W. J. Gallagher, M. B. Ketchen, A. W. Kleinsasser, R. H. Koch, S. I. Raider, and R. L. Sandstrom. Low-frequency noise in low $1/f$ noise dc squids. *APL*, 49:1393–1395, 1986.

[60] M. Kenyon, C. J. Lobb, and F. C. Wellstood. Temperature dependence of low-frequency noise in Al-Al_2O_3-Al single-electron transistors. *Jour. Appl. Phys.*, 88:6536, 2000.

[61] O. Astafiev, Yu. A. Pashkin, Y. Nakamura, T. Yamamoto, and J. S. Tsai. Temperature square dependence of the low frequency $1/f$ charge noise in the josephson junction qubits. *PRL*, 96:137001, 2006.

[62] Quantum Design Corp., 2001. Quantum Design Model 50 sensor with Model 550 and Model 5000 controller.

[63] F. C. Wellstood, C. Urbina, and John Clarke. Hot-electron effects in metals. *PRB*, 49:5942, 1994.

[64] M. M. Khapaev. 3D-MLSI: The program for extraction of 3D inductances of multilayer superconductor circuits, 2007.

[65] A. N. Vystavkin et al. *Phys. Rev. Appl.*, 9:79, 1974.

[66] R. W. Simmonds, K. M. Lang, D. A. Hite, S. Nam, D. P. Pappas, and John M. Martinis. Decoherence in josephson phase qubits from junction resonators. *PRL*, 93:077003, 2004.